

TECHNICAL UNIVERSITY OF CRETE  
SCHOOL OF ELECTRICAL AND COMPUTER ENGINEERING  
TELECOMMUNICATIONS DIVISION



**Performance Analysis, Middleware &  
Hardware for Bistatic, Ultra-low Power  
Scatter Radio Networks**

by

Konstantinos Tountas

A THESIS SUBMITTED IN PARTIAL FULFILLMENT OF  
THE REQUIREMENTS FOR THE MASTER OF  
ELECTRICAL AND COMPUTER ENGINEERING

July 2016

THESIS COMMITTEE

Associate Professor Aggelos Bletsas, *Thesis Supervisor*

Associate Professor George N. Karystinos

Associate Professor Antonios Deligiannakis

# Abstract

For environmental sensing applications that require dense deployments, scatter radio is a promising communication scheme; since modulation is achieved by means of reflection, ultra low-cost and ultra-power RF front-ends are possible. However, scatter radio utilization in sensor networks has been limited, since commercial scatter radio applications, like Radio Frequency Identification (RFID), are limited to ranges of a few meters. This work compares the two most prominent scatter radio architectures, namely the monostatic and the bistatic, exploiting both communication and microwave theory basics. The comparison metrics include the bit error rate (BER) under maximum-likelihood detection for the single-user case and the outage probability for the multi-user (network) case. Exact BER and tight, tag/sensor-topology independent outage probability bounds based on the Jensen inequality are derived for Rayleigh fading, in both monostatic and bistatic scatter radio networks/architectures. It is shown that the bistatic architecture improves field coverage and system reliability, compared to monostatic, for scatter wireless sensor networks (WSNs). Based on this observation, a complete, low-cost, embedded, digital, bistatic scatter radio sensor network, perhaps the first of its kind, using frequency-shift keying (FSK) modulation and frequency division multiplexing (FDM), along with randomized time division multiplexing (TDM), is implemented and demonstrated. This work is perhaps a concrete step towards ultra-large scale, scatter radio sensor networks and relevant low-cost environmental monitoring applications.

Acknowledgments: This work was supported by the ERC04-BLASE project, executed in the context of the “Education & Lifelong Learning” Operational Program of the National Strategic Reference Framework (NSRF), General Secretariat for Research & Technology (GSRT), funded through European Union-European Social Fund and Greek national funds.

Thesis Supervisor: Associate Professor Aggelos Bletsas

# Acknowledgements

As my studies in Greece are coming to an end, I must say that the past years have been really special to me. Lots of ups and downs, loads of work, and loads of fun. Associate Prof. Aggelos Bletsas, was my mentor and was like a father to me. He opened my way in the world of research, and I owe him my way of thinking and everything I know. My dear friends and colleagues J. Kimionis, E. Kampianakis, N. Kargas, and P. N. Alevizos were the people that supported me, guided me, and worked with me throughout both my undergraduate and graduate studies. I. P. Athanasiou, S. Stefanakis and G. Antonopoulos are the closest thing I have to brothers. My family supported me and encouraged me every single day. Last but not least, my girlfriend Nota has been my best friend and the person who believed the most in me. I thank them all for believing in me. I now start my Ph.D. studies in the University at Buffalo, NY, with great experiences and beautiful moments in my mind and heart.

The greatest challenges lie ahead.

*To Nota.*

# Table of Contents

<b>Table of Contents</b> . . . . .	4
<b>List of Figures</b> . . . . .	6
<b>1 Introduction</b> . . . . .	8
1.1 Ultra-Large Scale Wireless Sensor Networks . . . . .	8
<b>2 Scatter Radio Analysis</b> . . . . .	12
2.1 Multiple User System Model . . . . .	12
2.1.1 Scatter Wireless Propagation Channel . . . . .	12
2.1.2 Bistatic System Model . . . . .	14
2.1.3 Monostatic System Model . . . . .	18
2.2 Why Bistatic . . . . .	20
2.2.1 Probability of Bit Error Under ML Coherent Detection . . . . .	20
2.3 BER Under ML Coherent Detection . . . . .	20
2.3.1 Outage Probability . . . . .	23
2.4 Outage Probability . . . . .	23
2.4.1 Monostatic Case . . . . .	23
<b>3 Implementing a Bistatic Scatter Radio Network</b> . . . . .	28
3.1 Network Components Overview . . . . .	28
3.2 Scatter Tag Implementation . . . . .	28
3.2.1 Scatter Board . . . . .	29
3.2.2 Power Board . . . . .	34
3.2.3 Sensor Board . . . . .	35
3.3 Carrier Emitter Network - Cellular Architecture . . . . .	37
3.4 Software Defined Radio Reader . . . . .	38
3.4.1 MATLAB Implementation . . . . .	38
3.4.2 GNURadio Implementation . . . . .	39
<b>4 Simulation and Experimental Results</b> . . . . .	41
4.1 Numerical Results . . . . .	41
4.2 Experimental Results . . . . .	48

---

4.2.1 Coverage . . . . .	48
4.2.2 Sensing . . . . .	50
<b>5 Conclusion &amp; Future Work . . . . .</b>	<b>52</b>
5.1 Conclusion . . . . .	52
5.2 Future Work . . . . .	53
<b>6 Appendix . . . . .</b>	<b>54</b>
6.1 RF Scatter Board Schematics & Bill of Materials . . . . .	54
6.2 Power Board Schematics & Bill of Materials . . . . .	57
6.3 Sensor Board Schematics & Bill of Materials . . . . .	59
<b>Bibliography . . . . .</b>	<b>63</b>

# List of Figures

1.1	Scatter radio modulation with a RF transistor. . . . .	9
2.1	Left: Bistatic channel model. Right: Monostatic channel model. . . . .	13
2.2	Multi-user bistatic channel model over the $l$ -th time slot. . . . .	15
2.3	Multi-user scatter BFSK signal processing chain. After CFO compensation and DC blocking, detection is performed at each user's correlator block output. . . . .	18
3.1	First semi-passive tag prototype. A commercial MCU development kit was used, with a custom made front end PCB. . . . .	29
3.2	Second RF tag prototypes, where all the components are on the same board. . . . .	30
3.3	Final version of the scatter radio tag. . . . .	30
3.4	The scatter sensor node in the tomato casing. . . . .	31
3.5	The FDM scheme used for the tags' MAC protocol. . . . .	34
3.6	Spectrum of five tags transmitting simultaneously. . . . .	35
3.7	The schematic of the power board. A simple OR function between two power sources. . . . .	36
3.8	The schematic of the power board. A simple OR function between two power sources. . . . .	36
3.9	Scatter radio field with sensors/RF tags. Multiple carrier emitters are placed in the field to illuminate tags, along with a centralized receiver/reader. . . . .	37
3.10	Simulation setup 2. The emitter is placed on the edge of the field and the tag-of-interest is moved away from the emitter, while the two interferers are closer to the emitter and the reader. . . . .	39
3.11	Simulation setup 2. The emitter is placed on the edge of the field and the tag-of-interest is moved away from the emitter, while the two interferers are closer to the emitter and the reader. . . . .	40
4.1	BER performance under ML coherent detection for monostatic and bistatic architecture. . . . .	42



# Chapter 1

## Introduction

### 1.1 Ultra-Large Scale Wireless Sensor Networks

In the modern era the conservation of the environment is very important. The unscrupulous exploitation of the planet's natural resources creates a huge environmental problem, making the monitoring of the environment a necessity. Agriculture is a human endeavour that requires constant monitoring in order to conserve water and keeping the soil's concentration of fertilisers in normal levels. This type of agriculture is called "precision agriculture". With precision agriculture, the watering and fertilizing schedules change according to the information about the soil's moisture and minerals and each plant's condition. Using these data correctly results in natural resources conservation and production growth. Typical monitoring technologies utilize nodes connected by myriad wires. Instead, wireless sensor networks (WSNs) can be utilized for large-scale monitoring, providing sensor measurements at high temporal and spatial resolution, transferring the data wirelessly, while utilizing small sized nodes. The WSN nodes utilize low-cost, low-power, feature-rich micro-controllers with analog and digital inputs, on which the sensors can be attached. The variety of environmental sensors is large, from soil moisture and air temperature to soil PH and chlorophyll levels. Such applications require ultra dense networks consisting of thousands of nodes to report information about each plant's *microclimate*.

The existing commercial WSN technologies use typical Marconi-type radio for wireless connectivity, such as ZigBee, Bluetooth, 802.11 and LoRa. These radios are usually expensive and energy consuming, because they consist of complex *active* radio frequency (RF) components. Typically, such a radio consists of amplifiers, mixers, phase locked loops (PLLs) and high quality filters. All these components increase the per node cost along with the energy demands, thus prohibiting the scalability of a WSN to dense network levels.

In order to create ultra-low power and ultra-low cost WSNs a different approach is needed. Scatter radio, i.e., communication by means of reflection rather than radiation, has been recently proposed as a viable solution for WSN communication [1]. This communication scheme is not a new idea; the first principles were proposed in 1948 [2]. In scatter radio, a single Marconi radio, called carrier emitter (CE), can be used, to illuminate the tags/sensor nodes. The modulation of the information at

the tags, is achieved by terminating the antenna between two loads; that way, the incident CE's signal is reflected with altered phase and/or amplitude, according to the load selected each time. In practice, load switching is achieved by switching a *single* RF transistor. When the transistor is switched to the high state, the antenna is short-circuited and any incident signal is scattered back with  $\pi$  radians phase change. Respectively, when the transistor is switched to the low state, the antenna is open-circuited and the incident signal is scattered back intact. This scheme is depicted in Fig.1.1

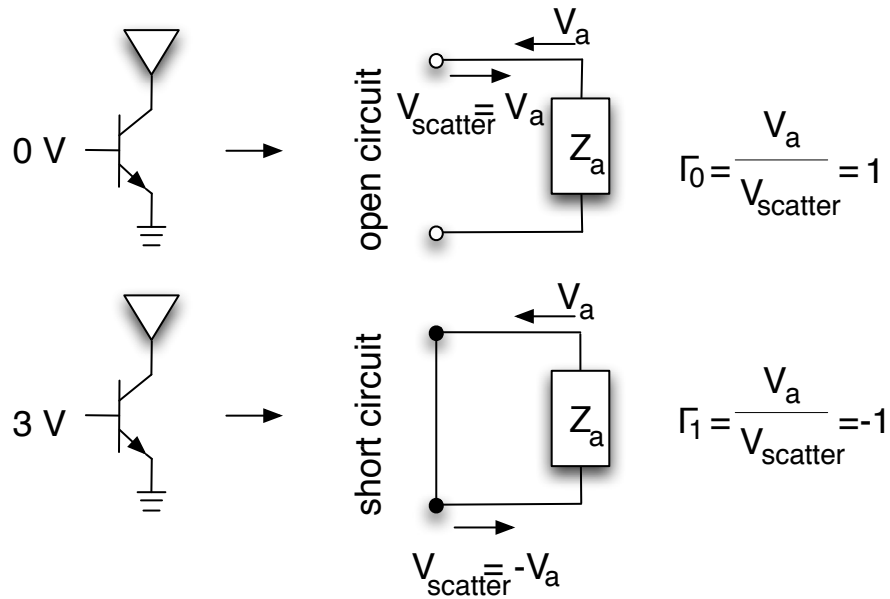


Figure 1.1: Scatter radio modulation with a RF transistor.

Nowadays, the most prominent commercial use of scatter radio is in radio frequency identification (RFID), widely used for inventorying, electronic tickets, people identification [3] or even musical instruments [4, 5]. Current industry standards (such as UHF EPC Class 1 Generation 2 [6]) focus on the aforementioned applications, disregarding the value of scatter radio in WSNs. Since communication can be achieved with a single RF transistor front end, the simplicity of the front-end minimizes the energy and monetary costs of each node. This allows the deployment of large-scale sensor networks; such networks are critical to applications like precision agriculture, where the environmental conditions of each plant, or among a small group of plants must be closely monitored. Proof of concept systems utilizing scatter radio in WSNs have been presented in [1, 7–11].

In precision agriculture, the nodes (or *tags*) must cover a vast area, hence the point-to-point links between the tags and the reader must be maximized. The two most prominent architectures of scatter networks are the monostatic, and the bistatic, depicted in Fig 2.1. Typical RFID applications utilize the monostatic architecture,

along with passive tags and high bit-rate communication. In the monostatic architecture the reader box consists of both the receiver, responsible for decoding the tag-modulated signals, and the modulated signal transmitter, responsible for the tag's powering. This means that typical RFID systems suffer from round-trip path loss. The standard also utilizes passive tags, which require a rectification circuit to convert the RF signals captured by the tag antenna to DC voltage that can drive the tag's digital logic. The RF signal used for powering is an modulated reader-transmitted signal. Thus, the achievable range of the point to point links is limited by the "power-up" link [12], and is limited to only a few meters. Moreover, the commercial tags implement high bit-rate communication for the tag-to-reader link, in the order of a few hundreds of kbps. This results in small bit duration, thus reduced energy-per-bit and signal-to-noise ratio (SNR), and ultimately reducing the communication range.

On the other hand, in the bistatic architecture the reader and the emitter are not co-located. By dislocating these two components, new, and more flexible topologies can be set up. CEs can come in the form of an oscillator and a power amplifier connected to an antenna, and thus be two orders of magnitude cheaper than the reader. The reader, can be a low-cost software defined radio (SDR), which offers the flexibility of decoding multiple tag communication schemes. One centralized reader can be placed in the field, while multiple low-cost carrier emitters (CEs) can be placed around it, surrounded by tags. Subsequently, the CE-to-tag link range is reduced, since each tag can be close to a CE with high probability. The use of multiple CEs allows the creation of a cell architecture between the emitters, allowing the reuse of the tags' frequencies. Furthermore, the use of semi-passive tags and low bitrates has been proposed, alongside the bistatic architecture with noncoherent [10] or coherent [13] signal processing, even with exploitation of short block-length channel codes [14], [15] to provide extended communication ranges. The semi-passive tags, i.e., energy assisted, power their electronics by batteries, or low cost renewable energy sources like low-voltage solar-cells [16]. Moreover, the bitrate should be minimized, to increase the energy-per-bit at the receiver, and thus the SNR.

Prior art has not investigated which architecture is more suitable for extended coverage and reliability of scatter sensor networks and rarely considers the bistatic architecture, focusing on the commercial-standard monostatic architecture. Examples toward the bistatic direction are [11, 17], in which the authors created analog bistatic scatter radio WSNs for air humidity, and soil moisture sensing, respectively. In [18] the authors suggest using a single CE with multiple readers-listeners that cooperate to decode tags simultaneously. That, however, does not lead towards coverage extension but is suggested as a mechanism for tag collision recovery and interference cancellation. The link budgets of both the monostatic and bistatic links were studied in-depth in [12]. Additionally, authors in [19] investigated the link-envelope correla-

---

tion of the dyadic backscatter channel (i.e., the most general backscatter channel), concluding that the use of separate transmitter and receiver antennas can reduce the point-to-point bit-error-rate (BER).

This work offers an analysis of the scatter radio architectures for scatter WSNs and provides an insight on the implementation aspects of a scatter radio WSN. Its main contribution points are:

- Presentation of the multiple user bistatic and monostatic signal models.
- Comparison of the monostatic and bistatic architectures in terms of BER under maximum-likelihood (ML) FSK detection for the single-user scenario [13].
- Comparison of the monostatic and bistatic architectures in terms of average probability of outage for the multi-user scenario, where tight Jensen-based upper bounds are derived. It is demonstrated that bistatic architecture achieves universally higher coverage compared to monostatic one over the family of grid networks.
- Experimental validation of the superiority of the bistatic architecture over the monostatic one, in terms of coverage and system reliability.
- Utilizing the bistatic architecture, a *digital* scatter radio WSN is demonstrated; it consists of ultra low-power, low-cost semi-passive tags employing FSK modulation and frequency-division multiplexing (FDM), as well as, a time-division multiplexing (TDM) scheme, allowing simultaneous, (almost) collision-free operation of multiple sensors-tags.

# Chapter 2

## Scatter Radio Analysis

In the following chapter, an extensive mathematical analysis of the two most prominent scatter radio architectures will be presented. In section 2.1 the system model of the bistatic topology will be derived. The system model of the monostatic topology will also be derived, as a special case of the bistatic. In section 2.2 the single user and the multiple user performance analysis of both the bistatic and the monostatic architectures will be presented.

### 2.1 Multiple User System Model

#### 2.1.1 Scatter Wireless Propagation Channel

A scatter radio network consisting of  $N$  *static* tags at distinct positions, scattering their measured data to a SDR reader. The set of all tags is defined as  $\mathcal{N} \triangleq \{1, 2, \dots, N\}$ .

For the bistatic architecture  $L$  CEs are assumed. The carrier emitters transmit a constant wave (CW) at a specific frequency, utilizing time-division multiplexing (TDM) as their MAC protocol. At each time slot only one CE is emitting a CW at the specific frequency. The set of all CEs is defined as  $\mathcal{L} \triangleq \{1, 2, \dots, l\}$ . It is very important to state that each CE emission is assumed to span more than the channel's coherence time period  $T_{\text{coh}}$ . For simplicity it will be assumed that the time duration of the  $l$ -th CE sinusoid signal (i.e. the  $l$ -th time slot) spans an integer number of  $T_{\text{coh}}$ . Each CE is a separate device placed away from the reader, as shown in Fig. 2.1-Left. Moreover, it is assumed that each tag transmits a single data packet during each time slot; the duration of the transmission is smaller than  $T_{\text{coh}}$ . The main goal of the network is to maximize the total coverage, thus the SDR reader has to be associated with many CEs, i.e.,  $L > 1$ . For the  $l$ -th time slot there are  $2N$  unidirectional links ( $N$  links between the CE and the tags, and  $N$  between the tags and the SDR reader). The distance between the  $l$ -th CE and the  $n$ -th tag is denoted by  $d_{C_l T_n}$ ,  $l \in \mathcal{L}$  and  $n \in \mathcal{N}$ , the distance between the  $n$ -th tag and the reader is denoted as  $d_{T_n R}$ ,  $n \in \mathcal{N}$ , while the distance between the  $l$ -th CE and the reader is denoted as  $d_{C_l R}$ ,  $l \in \mathcal{L}$ .

In the monostatic architecture the *single-antenna* reader functions as both the receiver and the CW emitter; the reader transmit the CW, illuminating the tags, which modulate their information on the incident signal and reflect the modulated signal

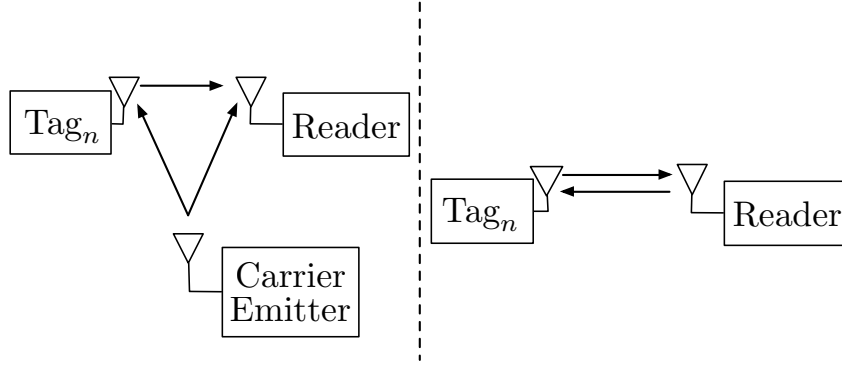


Figure 2.1: Left: Bistatic channel model. Right: Monostatic channel model.

back to the SDR reader. Since the CE and the reader are co-located,  $N$  bidirectional links exist ( $N$  links between the reader and the tags), as shown in Fig. 2.1-Right. The distance between the reader and the  $n$ -th tag is denoted by  $d_k$ , where  $k \in \{T_n R, R T_n\}$  denotes the direction of the link (tag-to-reader or reader-to-tag, respectively).

Let  $\mathbf{u}_{T_n}$ ,  $n \in \mathcal{N}$ ,  $\mathbf{u}_{C_l}$ ,  $l \in \mathcal{L}$ , and  $\mathbf{u}_R$ , be denoting the position of  $n$ -th tag,  $l$ -th CE, and SDR reader, respectively. Then  $d_{C_l R} = \|\mathbf{u}_{C_l} - \mathbf{u}_R\|_2$ ,  $d_{C_l T_n} = \|\mathbf{u}_{T_n} - \mathbf{u}_{C_l}\|_2$ , and  $d_{T_n R} = d_{R T_n} = \|\mathbf{u}_{T_n} - \mathbf{u}_R\|_2$ .

Both systems experience path-loss and small-scale fading. Taking into account the line-of-sight (LoS) path between the receive and the transmit antennas, as well as the reflection from the ground (two-ray model), the one-way path loss can be approximated by [1]:

$$\mathsf{L}_k = \begin{cases} \mathsf{G}_{T_x(k)} \mathsf{G}_{R_x(k)} \left( \frac{\lambda}{4\pi d_k} \right)^2, & \text{if } d_k < d_0(k) \\ \mathsf{G}_{T_x(k)} \mathsf{G}_{R_x(k)} \left( \frac{h_{T_x(k)} h_{R_x(k)}}{(d_k)^2} \right)^2, & \text{if } d_k \geq d_0(k), \end{cases} \quad (2.1)$$

where  $\mathsf{G}_{T_x(k)}$  and  $\mathsf{G}_{R_x(k)}$  are the antenna gains of transmitter and receiver of link  $k$ , respectively, with  $T_x(k)$  and  $R_x(k)$  be denoting the transmitter and receiver of link  $k$ , where  $k \in \{C_l R, C_l T_n, T_n R\}$  and  $k \in \{T_n R, R T_n\}$  for bistatic and monostatic topologies, respectively. Parameter  $d_0(k)$  is given by:

$$d_0(k) = \frac{4\pi h_{T_x(k)} h_{R_x(k)}}{\lambda}, \quad (2.2)$$

where  $h_{T_x(k)}$  and  $h_{R_x(k)}$  are the heights of the transmitter and the receiver, respectively, and  $\lambda$  denotes the wavelength. Note that for the monostatic topology  $\mathsf{L}_{T_n R} = \mathsf{L}_{R T_n}$ , due to  $d_{T_n R} = d_{R T_n}$ .

Frequency non-selective (flat fading) channels are assumed, since the communication bandwidth and the delay spread are relatively small. The complex baseband channel impulse response of each link is depicted in Fig. 2.1-Left and -Right for mono-

static and bistatic topologies, respectively. Complex channel gains for the  $l$ -th slot are given by:

$$h_{l,k}(t) = h_{l,k} = a_{l,k} e^{-j\phi_{l,k}}, \quad (2.3)$$

where  $k \in \{C_lR, C_lT_n, T_nR\}$  or  $k \in \{T_nR, RT_n\}$  for bistatic and monostatic topologies, respectively.  $a_{l,k} \in \mathbb{R}_+$  denotes the channel attenuation parameter and  $\phi_{l,k} \in [0, 2\pi)$  denotes the phase shift introduced by the propagation delay. The channel impulse response parameters change independently every  $T_{\text{coh}}$ .

Due to reciprocity theorem, the small scale fading parameters are the same for every  $T_{\text{coh}}$  seconds, i.e.,  $h_{l,T_nR} = h_{l,RT_n}$  (see Fig. 2.1-Right). Thus, assuming Rayleigh fading and monostatic architecture

$$h_{l,T_nR} = h_{l,RT_n} \sim \mathcal{CN}(0, 1), \quad (2.4)$$

which are independent and identically distributed (IID) across different time slots  $l$ , since each time slot spans more than one  $T_{\text{coh}}$ . In contrast, for bistatic system,  $h_{l,k}$  are IID across different  $k \in \{C_lR, C_lT_n, T_nR\}$  (see Fig. 2.1-Left). Thus, assuming Rayleigh fading and bistatic architecture

$$h_{l,k} \sim \mathcal{CN}(0, 1), \quad k \in \{C_lR, C_lT_n, T_nR\}, \quad (2.5)$$

where across different slots,  $\{h_{l,k}\}_{l \in \mathcal{L}}$  are also IID.

The probability density function (PDF) of the Rayleigh distribution is:

$$f_{|h_{l,k}|}(x) = \frac{2x}{\sigma_{l,k}^2} e^{-\frac{x^2}{\sigma_{l,k}^2}}, \quad (2.6)$$

,where in our case  $\sigma_{l,k}^2 = 1$ .

### 2.1.2 Bistatic System Model

For the bistatic architecture, the  $l$ -th CE transmits a continuous sinusoid wave at carrier frequency  $F_c$ , with complex baseband equivalent:

$$q_l^{[b]}(t) = \sqrt{2P_{C_l}} e^{-j(2\pi\Delta F_l t + \Delta\phi_l)}, \quad (2.7)$$

where  $P_{C_l}$  is the  $l$ -th CE transmitting power at passband and  $\Delta F_l$  and  $\Delta\phi_l$  model the frequency and phase offset between the  $l$ -th CE and the SDR reader, respectively. It is noted that carrier frequency offset (CFO), as well as carrier phase offset (CPO) are non-zero in the bistatic system due to the fact that CE and the SDR reader do not share the same system clock.

At the  $l$ -th slot (Fig. 2.2), each tag  $n \in \mathcal{N}$  is illuminated by the carrier wave

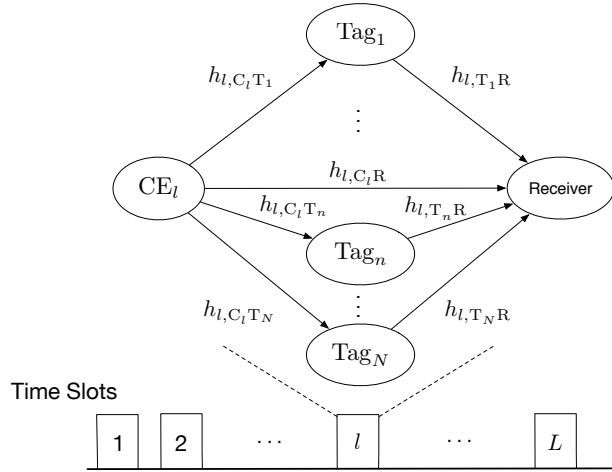


Figure 2.2: Multi-user bistatic channel model over the  $l$ -th time slot.

$q_l^{[b]}(t)$ , which is attenuated and rotated due to the channel  $\sqrt{L_{C_l T_n}} h_{l,C_l T_n}$ . The tag's information is modulated on the incident carrier wave by switching the antenna load between two loads, associated with two distinct reflection coefficients,  $\Gamma_{n,0}$  and  $\Gamma_{n,1}$ , for each bit. Hence, the baseband scattered waveform of user  $n$  can be written as:

$$u_{l,n}^{[b]}(t; i) = \mathbf{s}_n \left( \mathbf{v}_n + \frac{\Gamma_{n,0} - \Gamma_{n,1}}{2} b_n(t; i) \right) \cdot a_{l,C_l T_n} \sqrt{L_{C_l T_n}} e^{-j\phi_{l,C_l T_n}} q_l^{[b]}(t), i \in \{0, 1\}. \quad (2.8)$$

Parameter  $\mathbf{s}_n$  depends on the tag's inherent scattering efficiency and can be considered constant for a duration of  $L$  slots. The term  $\mathbf{v}_n$  is a DC constant that depends on the tag antenna structural mode  $A_s$ , as well as, the tag reflection coefficients  $\Gamma_{n,0}$ ,  $\Gamma_{n,1}$  [20].  $b_n(t; i)$  is a 50% duty cycle square waveform of frequency  $F_{n,i}$  and random initial phase  $\Phi_{n,i}$  [10]:  $b_n(t; i) = \frac{4}{\pi} \cos(2\pi F_{n,i} t + \Phi_{n,i}) \Pi_T(t)$ , for bit  $i \in \mathbb{B} \triangleq \{0, 1\}$ , where  $\Pi_T(t)$  is a rectangular pulse of bit duration  $T$ , i.e.,<sup>1</sup>

$$\Pi_T(t) = \begin{cases} 1, & 0 \leq t < T. \\ 0, & \text{otherwise.} \end{cases} \quad (2.9)$$

For a single bit duration  $T$ , the received demodulated complex baseband signal of the  $N$  tags over the  $l$ -th slot at the SDR reader is given by the sum of the superposition of the  $l$ -th carrier CW and each user's scattered signal through links  $C_l T_n$  and  $T_n R$ :  $y_l^{[b]}(t) = \sqrt{L_{C_l R}} h_{l,C_l R} q_l^{[b]}(t) + \sum_{n=1}^N \left( \sqrt{L_{T_n R}} h_{l,T_n R} u_{l,n}^{[b]}(t; i_n) \right) + w(t)$ . The additive term  $w(t)$  is a complex, circularly symmetric baseband additive Gaussian

<sup>1</sup>In practice, each backscattered bit depends on the time slot  $l$  because the sensed variable may change over time. This detail does not affect the proposed analysis and thus, it is omitted for notational convenience.

noise process, with power spectral density

$$S_w(F) = \begin{cases} N_0, & |F| \leq W_{\text{SDR}}, \\ 0, & \text{otherwise,} \end{cases} \quad (2.10)$$

where the parameter  $W_{\text{SDR}}$  stands for the SDR receiver's bandwidth.

If we substitute Eqs. (2.7) and (2.8) in the received signal  $y_i^{[b]}(t)$  a common CFO term  $\Delta F_l$  exists, that can be directly estimated using periodogram-based techniques and subsequently is compensated [10]. A DC term also exists on  $y_i^{[b]}(t)$  that can be estimated and removed from the signal by the received signal's time mean. Thus, the CFO-free, DC-blocked received signal over a bit period  $T$  of  $N$  tags can be written as [13, 15]:

$$\tilde{y}_l^{[b]}(t) = \sum_{n=1}^N \mu_{l,n}^{[b]} h_{l,n}^{[b]} \cos(2\pi F_{n,i_n} t + \Phi_{n,i_n}) \Pi_T(t) + w(t), \quad (2.11)$$

where the following abbreviations are utilized to obtain (2.12):  $\phi_{l,n}^{[b]} \triangleq \phi_{l,C_l T_n} + \phi_{l,T_n R} + \Delta\phi_l + \sqrt{\Gamma_{n,0} - \Gamma_{n,1}}$ ,  $a_{l,n}^{[b]} \triangleq a_{l,C_l T_n} a_{l,T_n R}$ ,  $h_{l,n}^{[b]} \triangleq a_{l,n}^{[b]} e^{-j\phi_{l,n}^{[b]}}$ , and  $\mu_{l,n}^{[b]} \triangleq \sqrt{2 P_{C_l} L_{C_l T_n} L_{T_n R} |\Gamma_{n,0} - \Gamma_{n,1}|} \frac{2}{\pi}$ .

The CFO-free, DC-blocked received signal at the reader over a bit period  $T$  of  $N$  tags can be written as [13, 15]:

$$\tilde{y}_l^{[b]}(t) = \sum_{n=1}^N \mu_{l,n}^{[b]} h_{l,n}^{[b]} \cos(2\pi F_{n,i_n} t + \Phi_{n,i_n}) \Pi_T(t) + w(t), \quad (2.12)$$

where the following abbreviations are utilized to obtain (2.12):  $\phi_{l,n}^{[b]} \triangleq \phi_{l,C_l T_n} + \phi_{l,T_n R} + \Delta\phi_l + \sqrt{\Gamma_{n,0} - \Gamma_{n,1}}$ ,  $a_{l,n}^{[b]} \triangleq a_{l,C_l T_n} a_{l,T_n R}$ ,  $h_{l,n}^{[b]} \triangleq a_{l,n}^{[b]} e^{-j\phi_{l,n}^{[b]}}$ , and  $\mu_{l,n}^{[b]} \triangleq \sqrt{2 P_{C_l} L_{C_l T_n} L_{T_n R} |\Gamma_{n,0} - \Gamma_{n,1}|} \frac{2}{\pi}$ .

The instantaneous received energy per bit for the bistatic system of tag  $n$  over the  $l$ -th slot, that is function of random amplitude  $a_{l,n}^{[b]}$ , is defined as [15]:

$$\mathbf{E}_{l,n}^{[b]}(a_{l,n}^{[b]}) \triangleq \frac{(\mu_{l,n}^{[b]} a_{l,n}^{[b]})^2 T}{2}. \quad (2.13)$$

Hence, for bistatic system the average received energy per bit of tag  $n$  over the  $l$ -th slot is

$$\mathbf{E}_{l,n}^{[b]} = \mathbb{E} \left[ \mathbf{E}_{l,n}^{[b]}(a_{l,n}^{[b]}) \right] = \frac{(\mu_{l,n}^{[b]})^2 T}{2}, \quad (2.14)$$

where  $\mathbb{E} \left[ (a_{l,n}^{[b]})^2 \right] = \mathbb{E}[(a_{l,C_l T_n})^2] \mathbb{E}[(a_{l,T_n R})^2] = 1$  was used. Finally, the average

received SNR of tag  $n$  at the  $l$ -th time slot for bistatic system is defined as

$$\text{SNR}_{l,n}^{[b]} \triangleq \frac{E_{l,n}^{[b]}}{N_0}. \quad (2.15)$$

### FSK Demodulation and FDM

The signal in Eq. (2.12) is the superposition of the  $N$  signals; each of them involves a cosine term which can be further expanded as:

$$\cos(2\pi F_{n,i_n} t) = \frac{1}{2} (e^{j2\pi F_{n,i_n} t} + e^{-j2\pi F_{n,i_n} t}), i_n \in \mathbb{B}. \quad (2.16)$$

Thus, from Eq. (2.16) we note that each tag  $n$  uses a unique set of subcarrier frequencies  $\pm F_{n,i_n}, i_n \in \mathbb{B}$  to scatter its information. In contrast to classic FSK, the negative frequencies  $-F_{n,0}$  and  $-F_{n,1}$  contribute to the total signal and thus, backscatter FSK modulation uses 4 frequencies,  $\pm F_{n,i_n}, i_n \in \mathbb{B}$ . Therefore, the classic FSK demodulator can not be used, since this will result to 3 dB loss in performance [10]. In a network level, the  $4N$  frequencies  $\{\pm F_{n,i_n}\}, \forall (i_n, n) \in \mathbb{B} \times \mathcal{N}$  must satisfy the orthogonality criterion, which for noncoherent FSK adheres to the following:<sup>2</sup>

$$|F_{n,i_n} - F_{j,i_j}| = \frac{k}{T} \quad \text{and} \quad F_{n,i_n} \gg \frac{1}{T}, \quad (2.17)$$

$\forall (i_n, n), (i_j, j) \in \mathbb{B} \times \mathcal{N} : (i_n, n) \neq (i_j, j)$ , and  $k \in \mathbb{N}$ . If the utilized frequencies satisfy (2.17), it can be shown that [10]:

$$\int_T e^{j2\pi F_{n,i_n} t} (e^{j2\pi F_{j,i_j} t})^* dt \approx \begin{cases} T, & F_{n,i_n} = F_{j,i_j}, \\ 0, & \text{otherwise,} \end{cases} \quad (2.18)$$

where the integration is performed over one bit period  $T$ . In view of Eq. (2.18), for each  $n \in \mathcal{N}$ , the set of time-limited in  $[0, T)$  exponentials of frequencies  $\{\pm F_{n,i}\}_{i \in \mathbb{B}}$ , normalized by  $\sqrt{T}$ , constitute an orthonormal basis of dimension 4. In addition, due to Eq. (2.18), for any  $n, j \in \mathcal{N}$  with  $n \neq j$ , the basis functions associated with frequencies  $\{\pm F_{n,i_n}\}_{i_n \in \mathbb{B}}$  and  $\{\pm F_{j,i_j}\}_{i_j \in \mathbb{B}}$  are orthogonal. This implies that the system of  $N$  users transmitting simultaneously can be divided into  $N$  parallel (i.e., independent) channels, where each user can be served separately from the others. As a result, single-tag detection techniques can be applied on each user separately, without affecting the rest ones. Such single-tag detection techniques have been extensively covered in [10, 13, 15].

Thus, the received signal in (2.12) passes through a bank of  $N$  correlation blocks; each block consists of 4 correlators, one for each frequency  $\pm F_{n,0}, \pm F_{n,1}, n \in \mathcal{N}$ , and

<sup>2</sup>For the coherent FSK term  $k/T$  in (2.17) is replaced with  $k/2T$ .

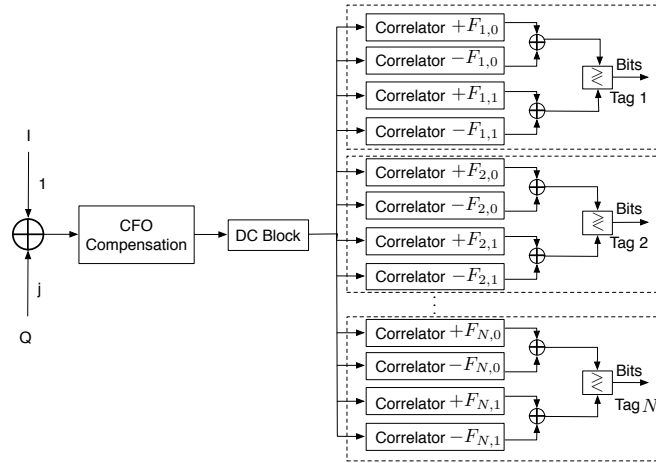


Figure 2.3: Multi-user scatter BFSK signal processing chain. After CFO compensation and DC blocking, detection is performed at each user's correlator block output.

the output of the  $n$ -th correlation block, over bit period  $T$ , is given by [15]:

$$\mathbf{r}_{l,n}^{[b]} = h_{l,n}^{[b]} \sqrt{E_{l,n}^{[b]}} \mathbf{x}_n + \mathbf{w}, \quad n \in \mathcal{N}, \quad (2.19)$$

where the vector  $\mathbf{x}_n$  is defined as:

$$\mathbf{x}_n \triangleq \sqrt{\frac{1}{2}} \begin{bmatrix} e^{+j\Phi_{n,0}} \\ e^{-j\Phi_{n,0}} \\ e^{+j\Phi_{n,1}} \\ e^{-j\Phi_{n,1}} \end{bmatrix} \odot \mathbf{u}_{i_n}, \quad n \in \mathcal{N}, \quad (2.20)$$

with  $\mathbf{u}_{i_n} = [(1 - i_n) \ (1 - i_n) \ i_n \ i_n]^\top$  is the four dimensional transmitted symbol of the  $n$ -th tag corresponding to transmitted bit  $i_n \in \mathbb{B}$ . For  $F_{n,i_n} + \frac{20}{T} \ll W_{\text{SDR}}$ ,  $\mathbf{w} \sim \mathcal{CN}(\mathbf{0}_4, N_0 \mathbf{I}_4)$  [13]. Symbol  $\odot$  denotes the component-wise (Hadamard) product. The signal processing chain of the multiple user BFSK used at the receiver is shown in Fig. 2.3.

### 2.1.3 Monostatic System Model

With bistatic system model derived above, the monostatic one can be approached as a special case of bistatic. Since, the SDR reader and the CE are co-located in the same reader-box, they share the same clock. Again, the reader transmits a continuous sinusoid wave at carrier frequency  $F_c$  and power  $P_R$  and due to the fact that the receiver and the emitter share the same system clock, the CFO  $\Delta F_l$  and the phase offset  $\Delta \phi_l$  are nonexistent, i.e., SDR reader emits  $q^{[m]}(t) = \sqrt{2P_R}$ .

Each tag modulates its information on the incident CW, using BFSK modulation. Following the same reasoning with the derivation of Eq. (2.12), and exploiting the

reciprocity of the channel between the reader and each tag, the DC-blocked received signal for monostatic system can be expressed as

$$\tilde{y}_l^{[m]}(t) = \sum_{n=1}^N \mu_n^{[m]} h_{l,n}^{[m]} \cos(2\pi F_{n,i_n} t + \Phi_{n,i_n}) \Pi_T(t) + w(t), \quad (2.21)$$

where the following abbreviations are employed in (2.21):  $a_{l,n}^{[m]} \triangleq (a_{l,T_nR})^2$ ,  $\phi_{l,n}^{[m]} \triangleq 2\phi_{l,T_nR} + \sqrt{\Gamma_{n,0} - \Gamma_{n,1}}$ ,  $\mu_n^{[m]} \triangleq \sqrt{2P_R} L_{T_nR} |\Gamma_{n,0} - \Gamma_{n,1}| \frac{2}{\pi} \mathbf{s}_n$ , and  $h_{l,n}^{[m]} \triangleq a_{l,n}^{[m]} e^{-j\phi_{l,n}^{[m]}}$ .

Accordingly to the bistatic setup, for each tag  $n$  the following quantities are utilized

$$\mathbf{E}_{l,n}^{[m]}(a_{l,n}^{[m]}) \triangleq \frac{(\mu_n^{[m]} a_{l,n}^{[m]})^2 T}{2}, \quad (2.22)$$

$$\mathbf{E}_n^{[m]} = \mathbb{E} \left[ \mathbf{E}_{l,n}^{[m]}(a_{l,n}^{[m]}) \right] = (\mu_n^{[m]})^2 T, \quad (2.23)$$

$$\text{SNR}_n^{[m]} \triangleq \frac{\mathbf{E}_n^{[m]}}{N_0}, \quad (2.24)$$

where in (2.23) we exploited the fact that  $\mathbb{E} \left[ (a_{l,n}^{[m]})^2 \right] = \mathbb{E} [(a_{l,T_nR})^4] = 2$ .

**Remark 1.** It is emphasized that quantities  $\mathbf{E}_n^{[m]}$  and  $\text{SNR}_n^{[m]}$  above do not depend on time index  $l$ , because they are functions of path loss  $L_{T_nR}$  that remains unaffected during the  $L$  slots. In contrast, quantities  $\mathbf{E}_{l,n}^{[b]}$  and  $\text{SNR}_{l,n}^{[b]}$  in Eqs. (2.14) and (2.15), which are both functions of path loss  $L_{C_lT_n}$ , depend on the time slot index  $l$ , because at each different slot  $l$  different CE transmits. ■

Similarly to the bistatic case, the received signal in (2.21) can be processed concurrently by  $N$  parallel correlator blocks, associated with the  $N$  tags, with the way discussed in Section 2.1.2. The processing for the  $n$ -th tag projects the received signal  $\tilde{y}_l^{[m]}(t)$  onto basis  $\left\{ \frac{1}{\sqrt{T}} e^{\pm j2\pi F_{n,i_n} t} \Pi_T(t) \right\}_{i_n \in \mathbb{B}}$  and the received baseband signal over bit period  $T$  is given by

$$\mathbf{r}_{l,n}^{[m]} = h_{l,n}^{[m]} \sqrt{\frac{\mathbf{E}_n^{[m]}}{2}} \mathbf{x}_n + \mathbf{w}, \quad n \in \mathcal{N}, \quad (2.25)$$

where vector  $\mathbf{x}_n$  is given in (2.20), and for  $F_{n,i_n} + \frac{20}{T} \ll W_{\text{SDR}}$ ,  $\mathbf{w} \sim \mathcal{CN}(\mathbf{0}_4, N_0 \mathbf{I}_4)$ .

## 2.2 Why Bistatic

### 2.2.1 Probability of Bit Error Under ML Coherent Detection

In this section we try to seek the order of decay as a function of average received SNR of the probability of bit error as SNR goes to infinity, assuming that SDR reader implements coherent ML detection. This metric is also known as diversity order [21].

## 2.3 BER Under ML Coherent Detection

This section compares the diversity order [21] of monostatic vs bistatic system, assuming coherent, maximum likelihood (ML) detection.

### Monostatic Case

In the monostatic architecture, according to Eq. (2.25), for given channel realization  $h_{l,n}^{[m]}$ , the conditional probability of error for tag  $n$  over time slot  $l$  under ML coherent scatter radio FSK detection depends only on amplitude  $|h_{l,n}^{[m]}| = a_{l,n}^{[m]}$  and is given by [22, p. 508]:

$$\begin{aligned} \Pr(e_{l,n}^{[m]} | a_{l,n}^{[m]}) &= \mathbb{Q}\left(\frac{a_{l,n}^{[m]} \sqrt{\frac{E_n^{[m]}}{2}} \|\mathbf{x}_0 - \mathbf{x}_1\|_2}{\sqrt{2N_0}}\right) \\ &= \mathbb{Q}\left(a_{l,n}^{[m]} \sqrt{\frac{\text{SNR}_n^{[m]}}{2}}\right), \end{aligned} \quad (2.26)$$

where  $\mathbb{Q}(x) = \frac{1}{2\pi} \int_x^\infty e^{-\frac{t^2}{2}} dt$ ,  $x \in \mathbb{R}$  and  $\|\mathbf{x}_0 - \mathbf{x}_1\|_2 = \sqrt{2}$  as well as the SNR definition for monostatic systems in Eq. (2.24) were utilized.

Furthermore, in the monostatic case the wireless channels are fully correlated (cf. Eq. (2.3)) and random variable (RV)  $a_{l,n}^{[m]} = (a_{l,T_nR})^2$  follows the exponential distribution with  $\mathbb{E}[a_{l,n}^{[m]}] = 1$ . As a result, the unconditional probability of error over the  $l$ -th slot for the  $n$ -th tag is given by:

$$\begin{aligned} \Pr(e_{l,n}^{[m]}) &= \mathbb{E}_{a_{l,n}^{[m]}} \left[ \Pr(e_{l,n}^{[m]} | a_{l,n}^{[m]}) \right] = \int_0^\infty \mathbb{Q}\left(x \sqrt{\frac{\text{SNR}_n^{[m]}}{2}}\right) e^{-x} dx \\ &= \frac{1}{2} - e^{\frac{1}{\text{SNR}_n^{[m]}}} \mathbb{Q}\left(\sqrt{\frac{2}{\text{SNR}_n^{[m]}}}\right), \end{aligned} \quad (2.27)$$

where [23, Eqs. (7.14.2), (7.2.1), (7.2.2)] are utilized.

**Proposition 1.** Monostatic architecture offers diversity order of  $1/2$  for any  $(l, n) \in \mathcal{L} \times \mathcal{N}$ .

*Proof:* The diversity order for probability of error in (2.27) is given by [21]

$$\lim_{\text{SNR}_n^{[m]} \rightarrow \infty} \frac{\log\left(\Pr\left(e_{l,n}^{[m]}\right)\right)}{\log\left(\text{SNR}_n^{[m]}\right)} = \lim_{x \rightarrow 0} \frac{\log\left(\frac{1}{2} - e^x \text{Q}(\sqrt{2x})\right)}{\log\left(\frac{1}{x}\right)}.$$

By applying the rule of L'Hospital:

$$\lim_{x \rightarrow 0} \frac{-e^x \text{Q}(\sqrt{2x}) + \frac{1}{2\sqrt{\pi x}}}{-\frac{1}{x} \left[\frac{1}{2} - e^x \text{Q}(\sqrt{2x})\right]}. \quad (2.28)$$

Then by multiplying both the denominator and the numerator with  $e^{-x}$ :

$$\lim_{x \rightarrow 0} \frac{x \text{Q}(\sqrt{2x}) - \frac{e^{-x}\sqrt{x}}{2\sqrt{\pi}}}{\frac{e^{-x}}{2} - \text{Q}(\sqrt{2x})}. \quad (2.29)$$

Again, the rule of L'Hospital is applied :

$$\lim_{x \rightarrow 0} \frac{\text{Q}(\sqrt{2x}) - \frac{e^{-x}}{4\sqrt{\pi x}}}{-\frac{e^{-x}}{2} + \frac{e^{-x}}{2\sqrt{\pi x}}}. \quad (2.30)$$

Finally, by multiplying the denominator and the numerator with  $e^x \sqrt{x}$ :

$$\lim_{x \rightarrow 0} \frac{e^x \sqrt{x} \text{Q}(\sqrt{2x}) - \frac{1}{4\sqrt{\pi}}}{-\frac{\sqrt{x}}{2} + \frac{1}{2\sqrt{\pi}}} = -\frac{1}{2}. \quad (2.31)$$

The above result indicates that for any slot the bit error rate (BER) in the monostatic system decays inversely proportional with square root of SNR, at the high SNR regime. Below, it is shown that the decay is faster in the bistatic system.

### Bistatic Case

In the bistatic case, according to Eq. (2.19), the conditional BER for tag  $n$  over the  $l$ -th time slot can be simplified as:

$$\Pr\left(e_{l,n}^{[b]} \mid a_{l,n}^{[b]}\right) = \text{Q}\left(a_{l,n}^{[b]} \sqrt{\text{SNR}_{l,n}^{[b]}}\right), \quad (2.32)$$

where the definition of SNR in Eq. (2.15) was utilized. The above conditional probability can be upper bounded as follows:

$$\Pr\left(e_{l,n}^{[b]} \mid a_{l,n}^{[b]}\right) = \mathbb{Q}\left(a_{l,n}^{[b]} \sqrt{\text{SNR}_{l,n}^{[b]}}\right) \leq \frac{1}{2} e^{-\frac{(a_{l,n}^{[b]})^2 \text{SNR}_{l,n}^{[b]}}{2}}. \quad (2.33)$$

Since  $a_{l,n}^{[b]}$  is the product of two unit power Rayleigh distributed RVs, the probability of bit error can be upper bounded as follows:

$$\begin{aligned} \Pr\left(e_{l,n}^{[b]}\right) &= \mathbb{E}_{a_{l,n}^{[b]}} \left[ \Pr\left(e_{l,n}^{[b]} \mid a_{l,n}^{[b]}\right) \right] \\ &\stackrel{(2.33)}{\leq} \int_0^\infty \int_0^\infty \frac{1}{2} e^{(-x^2 y^2 \frac{1}{2} \text{SNR}_{l,n}^{[b]})} 4 x y e^{-x^2 - y^2} dx dy \end{aligned} \quad (2.34)$$

$$= \int_0^\infty 2 \frac{y e^{-y^2}}{2 + y^2 \text{SNR}_{l,n}^{[b]}} dy = \int_0^\infty \frac{e^{-y}}{2 + y \text{SNR}_{l,n}^{[b]}} dy \quad (2.35)$$

$$= \left( \frac{1}{\text{SNR}_{l,n}^{[b]}} \right) \exp\left( \frac{2}{\text{SNR}_{l,n}^{[b]}} \right) \Gamma\left(0, \frac{2}{\text{SNR}_{l,n}^{[b]}}\right), \quad (2.36)$$

where [24, Eq. (3.461.3)] and [24, Eq. (3.383.10)] are utilized to obtain Eqs. (2.35) and (2.36), respectively and  $\Gamma(a, x) \triangleq \int_x^\infty t^{a-1} e^{-t} dt$  is the upper incomplete gamma function.

**Proposition 2.** Bistatic architecture offers diversity order at least 1 for any  $(l, n) \in \mathcal{L} \times \mathcal{N}$ .

*Proof:* The diversity order for the upper bound in (2.36) is given by

$$\begin{aligned} &\lim_{x \rightarrow \infty} \frac{\log\left(\frac{1}{x} e^{\frac{2}{x}} \Gamma\left(0, \frac{2}{x}\right)\right)}{\log(x)} \\ &= \lim_{x \rightarrow \infty} \left[ \frac{\log\left(\frac{1}{x}\right)}{\log(x)} + \frac{\log\left(e^{\frac{2}{x}}\right)}{\log(x)} + \frac{\log\left(\Gamma\left(0, \frac{2}{x}\right)\right)}{\log(x)} \right]. \end{aligned} \quad (2.37)$$

By applying the L'Hospital's rule and [23, Eq. (8.8.13)]:

$$\begin{aligned} &\lim_{x \rightarrow \infty} \left[ \frac{\log\left(\frac{1}{x}\right)}{\log(x)} + \frac{2}{x \log(x)} + \frac{e^{-\frac{2}{x}}}{\Gamma\left(0, \frac{2}{x}\right)} \right] \\ &= -1 + \lim_{x \rightarrow \infty} \frac{e^{-\frac{2}{x}}}{\Gamma\left(0, \frac{2}{x}\right)}, \end{aligned} \quad (2.38)$$

where it was used that  $\lim_{x \rightarrow \infty} \frac{\log\left(\frac{1}{x}\right)}{\log(x)} = -1$ ,  $\lim_{x \rightarrow \infty} \frac{2}{x \log(x)} = 0$ , and  $\lim_{x \rightarrow \infty} \frac{e^{-\frac{2}{x}}}{\Gamma\left(0, \frac{2}{x}\right)} = \lim_{x \rightarrow 0} \frac{1}{\Gamma(0, 2x)} = 0$  due to [23, Eqs. (8.4.4), (6.6.2)].

Thus, it is concluded that in the bistatic system, the BER drops faster compared to the monostatic, at the high SNR regime.

### 2.3.1 Outage Probability

## 2.4 Outage Probability

In Section 2.1.1, it was assumed that all switching (subcarrier) frequencies used by the tags 1) are distinct and 2) adhere to the orthogonality criterion (Eq. (2.17)). In practice, the above conditions may not be always feasible, due to implementation constraints (e.g., clock drifts) and frequency generation constraints. As a result, tags that transmit simultaneously may produce interference to each other. The set  $\mathcal{A}(n)$  denotes the tags that interfere with the reception of tag  $n$ . Hence, the set of interferers with respect to tag  $n$  is given by  $\mathcal{A}(n) = \mathcal{N} \setminus \{n\}$ .

### 2.4.1 Monostatic Case

Let  $\mathcal{T}_N^{[m]} \triangleq \{\mathbf{u}_{T_n}\}_{n \in \mathcal{N}} \cup \{\mathbf{u}_R\}$  be a fixed, monostatic scatter radio architecture WSN topology. Incorporating imperfections as mentioned above, the signal-to-interference-plus-noise ratio (SINR) of tag  $n$  at the  $l$ -th time slot is given by:

$$\begin{aligned} \text{SINR}_{l,n}^{[m]} &\triangleq \frac{g_{l,n}^{[m]} \frac{\mathbf{E}_n^{[m]}}{2}}{\sum_{j \in \mathcal{A}(n)} \rho_{nj} g_{l,j}^{[m]} \frac{\mathbf{E}_j^{[m]}}{2} + N_0} \\ &= \frac{g_{l,n}^{[m]} \mathbf{E}_n^{[m]}}{\sum_{j \in \mathcal{A}(n)} \rho_{nj} g_{l,j}^{[m]} \mathbf{E}_j^{[m]} + 2N_0} \end{aligned} \quad (2.39)$$

where  $g_{l,n}^{[m]} \triangleq |h_{l,n}^{[m]}|^2 = \left(a_{l,n}^{[m]}\right)^2$  was defined. Parameter  $\rho_{nj}$  is inversely proportional to the subcarrier frequency separation between tag  $n$  and tag  $j$ ,  $j \in \mathcal{A}(n)$  [1] and depends on the spectral efficiency of the specific binary modulation implemented at each tag and the filtering functions at the reader:

$$\rho_{nj} = \max_{i_n, i_j \in \mathcal{B}} \left\{ \left[ \varepsilon_{n,j} |F_{n,i_n} - F_{j,i_j}| \right]^{-2} \right\}, \quad j \in \mathcal{A}(n), \quad (2.40)$$

where parameter  $\varepsilon_{n,j}$  is an approximation constant that also incorporates the mismatch between the clocks of tag  $n$  and  $j$ ; subcarrier frequency difference raised at the second power, as opposed to the fourth power, is due to the power spectral density of FSK implemented at each tag, as opposed to (continuous phase) minimum-shift keying (MSK) [1].

Since the monostatic compound channel amplitude  $a_{l,n}^{[m]}$  is exponentially distributed,

probability density function (PDF) of  $g_{l,n}^{[m]}$  is given by [25, p. 199]:  $f_{g_{l,n}^{[m]}}(x) = \frac{1}{2\sqrt{x}}e^{-\sqrt{x}}$ ,  $x \geq 0$ , and cumulative distribution function (CDF) is given by:

$$F_{g_{l,n}^{[m]}}(x) = \int_0^x f_{g_{l,n}^{[m]}}(y) dy = 1 - e^{-\sqrt{x}}, \quad x \geq 0. \quad (2.41)$$

In the monostatic topology  $\mathcal{T}_N^{[m]}$ , the outage event for the  $n$ -th user over  $L$  attempts (time slots), is the probability that the  $n$ -th tag/user's SINR is below threshold  $\theta$  over all  $L$  slots:

$$\Pr\left(\text{out}_{L,n}^{[m]} | \mathcal{T}_N^{[m]}, \theta\right) = \Pr\left(\bigcap_{l=1}^L \left\{ \text{SINR}_{l,n}^{[m]} \leq \theta \right\}\right) \quad (2.42)$$

$$\stackrel{(a)}{=} \left[ \Pr\left(\text{SINR}_{l,n}^{[m]} \leq \theta\right) \right]^L, \quad (2.43)$$

for  $l \in \mathcal{L}$ , where (a) is due to the fact that  $g_{l,n}^{[m]}$  are i.i.d. for all  $(l, n) \in \mathcal{L} \times \mathcal{N}$ .

Each probability in the product of Eq. (2.43) can be further analyzed as follows:

$$\begin{aligned} \Pr\left(\text{SINR}_{l,n}^{[m]} \leq \theta\right) &\stackrel{(a)}{=} \Pr\left(g_{l,n}^{[m]} \leq \frac{2\theta N_0}{\mathbf{E}_n^{[m]}} + \frac{\theta \mathbf{I}_{l,n}^{[m]}}{\mathbf{E}_n^{[m]}}\right) \\ &\stackrel{(b)}{\leq} F_{g_{l,n}^{[m]}}\left(\frac{2\theta N_0}{\mathbf{E}_n^{[m]}} + \frac{\theta \mathbb{E}\left[\mathbf{I}_{l,n}^{[m]}\right]}{\mathbf{E}_n^{[m]}}\right) \end{aligned} \quad (2.44)$$

$$\stackrel{(c)}{=} 1 - e^{-\sqrt{\frac{2\theta}{\text{SINR}_n^{[m]}}}} = F_{g_{l,n}^{[m]}}\left(\frac{2\theta}{\text{SINR}_n^{[m]}}\right), \quad (2.45)$$

for some  $l \in \mathcal{L}$ . In (a), total interference at tag  $n$  for the monostatic system at the  $l$ -th time slot was defined as  $\mathbf{I}_{l,n}^{[m]} \triangleq \sum_{j \in \mathcal{A}(n)} \rho_{nj} g_{l,j}^{[m]} \mathbf{E}_j^{[m]}$ ; in (b), the law of iterated expectation [26] alongside with Jensen's inequality was utilized, by exploiting the concavity of the function in Eq. (2.41); in (c), the linearity of expectation was exploited, plugging in the average received SINR, defined as:

$$\begin{aligned} \text{SINR}_n^{[m]} &\triangleq \frac{\mathbb{E}\left[g_{l,n}^{[m]}\right] \mathbf{E}_n^{[m]}}{\sum_{j \in \mathcal{A}(n)} \rho_{nj} \mathbb{E}\left[g_{l,j}^{[m]}\right] \mathbf{E}_j^{[m]} + 2N_0} \\ &= \frac{\mathbf{E}_n^{[m]}}{\sum_{j \in \mathcal{A}(n)} \rho_{nj} \mathbf{E}_j^{[m]} + N_0}. \end{aligned} \quad (2.46)$$

Finally, for fixed topology  $\mathcal{T}_N^{[m]}$ , the average outage probability of the monostatic

system across all tags, is expressed as:

$$\Pr\left(\overline{\text{out}}_L^{[m]} | \mathcal{T}_N^{[m]}, \theta\right) = \frac{1}{N} \sum_{n=1}^N \Pr\left(\text{out}_{L,n}^{[m]} | \mathcal{T}_N^{[m]}, \theta\right) \quad (2.47)$$

$$\stackrel{(2.45)}{\leq} \frac{1}{N} \sum_{n=1}^N \left[ F_{g_{l,n}^{[m]}} \left( \frac{2\theta}{\text{SINR}_n^{[m]}} \right) \right]^L. \quad (2.48)$$

### Bistatic Case

For fixed bistatic topology, consisting of  $N$  tags and  $L$  CEs, defined as  $\mathcal{T}_{L,N}^{[b]} \triangleq \{\mathbf{u}_{T_n}\}_{n \in \mathcal{N}} \cup \{\mathbf{u}_{C_l}\}_{l \in \mathcal{L}} \cup \{\mathbf{u}_R\}$ , the instantaneous SINR of tag  $n$  for the  $l$ -th time slot, is given by:

$$\text{SINR}_{l,n}^{[b]} \triangleq \frac{g_{l,n}^{[b]} \mathbf{E}_{l,n}^{[b]}}{\sum_{j \in \mathcal{A}(n)} \rho_{nj} g_{l,j}^{[b]} \mathbf{E}_{l,j}^{[b]} + N_0}, \quad (2.49)$$

where RV  $g_{l,n}^{[b]} \triangleq \left(a_{l,n}^{[b]}\right)^2$  is defined. As in the monostatic case, the interference for tag  $n$  at the  $l$ -th time in the bistatic system is defined as  $I_{l,n}^{[b]} \triangleq \sum_{j \in \mathcal{A}(n)} \rho_{nj} g_{l,j}^{[b]} \mathbf{E}_{l,j}^{[b]}$ . The PDF of  $a_{l,n}^{[b]}$  is given by [19, Eq. (3)]:  $f_{a_{l,n}^{[b]}}(x) = 4x \mathbf{K}_0(2x)$ ,  $x \geq 0$ , where  $\mathbf{K}_0(x) = \int_0^\infty \frac{\cos(xt)}{\sqrt{t^2+1}} dt$ ,  $x > 0$ , is the zero-order modified Bessel function of the second kind [23, Eq. 10.32.6]. Using [25, p. 199], the PDF of  $g_{l,n}^{[b]}$  is given by:  $f_{g_{l,n}^{[b]}}(x) = 2 \mathbf{K}_0(2\sqrt{x})$ ,  $x \geq 0$ , and the corresponding CDF follows:

$$\begin{aligned} F_{g_{l,n}^{[b]}}(x) &= \int_0^x f_{g_{l,n}^{[b]}}(y) dy = \int_0^x 2 \mathbf{K}_0(2\sqrt{y}) dy \\ &\stackrel{(a)}{=} \int_0^{2\sqrt{x}} z \mathbf{K}_0(z) dz \stackrel{(b)}{=} 4x \int_0^1 y \mathbf{K}_0(2\sqrt{x}y) dy \\ &\stackrel{(c)}{=} 1 - 2\sqrt{x} \mathbf{K}_1(2\sqrt{x}), \quad x \geq 0, \end{aligned} \quad (2.50)$$

where in (a) it was used that  $2\sqrt{y} = z$ , in (b)  $\frac{z}{2\sqrt{x}} = y$ , in (c) [19, Eq. (6.561.8)] was used, and  $\mathbf{K}_1(\cdot)$  is the first-order modified Bessel function of the second kind [23, Eq. (10.32.9)] with  $\nu = 1$ . Applying similar reasoning as in the monostatic case, for fixed bistatic topology  $\mathcal{T}_{L,N}^{[b]}$  and threshold  $\theta$ , the outage probability of tag  $n$  operating over  $L$  time slots can be expressed as follows:

$$\Pr\left(\text{out}_{L,n}^{[b]} | \mathcal{T}_{L,N}^{[b]}, \theta\right) \stackrel{(a)}{=} \prod_{l=1}^L \Pr\left(\text{SINR}_{l,n}^{[b]} \leq \theta\right), \quad (2.51)$$

where in (a), the independence of RVs  $\left\{\text{SINR}_{l,n}^{[b]}\right\}_{l \in \mathcal{L}}$  was exploited. It is noted that these RVs are not identically distributed, as discussed in Remark 1. In order to use the same reasoning with the derivation in Eq. (2.45)  $F_{g_{l,n}^{[b]}}$  must be a concave function.

*Proof:* By differentiating the CDF  $F_{g_{l,n}^{[b]}}(x)$  with respect to  $x$  the PDF  $f_{g_{l,n}^{[b]}}(x) = 2\mathbf{K}_0(2\sqrt{x})$ ,  $x \geq 0$  is obtained.

By differentiating the PDF, and using [23, Eq. (10.29.3)] the second order derivative is obtained:

$$\frac{d}{dx} f_{g_{l,n}^{[b]}}(x) = \frac{d}{dx} 2\mathbf{K}_0(2\sqrt{x}) = -\frac{2\mathbf{K}_1(2\sqrt{x})}{\sqrt{x}}. \quad (2.52)$$

The second order derivative is always negative since  $\mathbf{K}_1(x) > 0, \forall x > 0$  and  $\sqrt{x} > 0, \forall x > 0$ . Hence,  $F_{g_{l,n}^{[b]}}$  is concave.

Again, by using the same reasoning with the derivation in Eq. (2.45), alongside the concavity of  $F_{g_{l,n}^{[b]}}$ , the following is obtained:

$$\Pr\left(\text{SINR}_{l,n}^{[b]} \leq \theta\right) \leq F_{g_{l,n}^{[b]}}\left(\frac{\theta}{\text{SINR}_{l,n}^{[b]}}\right) \quad (2.53)$$

with

$$\text{SINR}_{l,n}^{[b]} \triangleq \frac{\mathbf{E}_{l,n}^{[b]}}{\sum_{j \in \mathcal{A}(n)} \rho_{nj} \mathbf{E}_{l,j}^{[b]} + N_0}. \quad (2.54)$$

The average outage probability in the bistatic system can be upper bounded as follows:

$$\Pr\left(\overline{\text{out}}_L^{[b]} | \mathcal{T}_{L,N}^{[b]}, \theta\right) \stackrel{(2.53)}{\leq} \frac{1}{N} \sum_{n=1}^N \prod_{l=1}^L F_{g_{l,n}^{[b]}}\left(\frac{\theta}{\text{SINR}_{l,n}^{[b]}}\right). \quad (2.55)$$

**Remark 2.** It is noted that the moment generating function (MGF) of RVs  $g_{l,n}^{[m]}$  and  $g_{l,n}^{[b]}$ ,  $\forall (l, n) \in \mathcal{L} \times \mathcal{N}$ , does not exist, and thus, bounds of average outage probability through Chernoff-bound techniques are not readily available. ■

### Average Outage Probability over Square Grid Networks

Observing Eqs. (2.47) and (2.55), it is immediately apparent that both depend on a fixed topology. In order to obtain a topology-independent, universal outage probability, an expression that averages over possible topologies has to be obtained. Since, there are infinite classes of topologies to choose from, our attention is restricted to the class of square  $M \times M$  grid network topologies, that are tractable for analysis and are used in practice. These topologies are parametrized also by grid resolution  $\Delta$ ; both  $M$  and  $\Delta$  have meter units.<sup>3</sup> For simplicity, it is assumed that  $\Delta$  divides  $M$ , i.e.,  $M/\Delta = K \in \mathbf{N}$ . The following network is considered, as the most representative

<sup>3</sup>The analysis here is carried out over square (equal size per side) 2-dimensional (2D) grid topologies, but it can be extended to more dimensions, rectangular networks and unequal grid resolution per dimension.

and intuitive example belonging to the above class

$$\mathcal{G}_{M,\Delta} = \left\{ [k_1\Delta \quad k_2\Delta]^\top : (k_1, k_2) \in \{0, 1, \dots, K\}^2 \right\}. \quad (2.56)$$

Set  $\mathcal{G}_{M,\Delta}$  has  $(K+1)^2$  elements (2D grid points). Let  $M$  and  $\Delta$  be chosen so that  $(K+1)^2 \geq N+L+1$ .

For a monostatic system with fixed SDR reader's position  $\mathbf{u}_R \in \mathcal{G}_{M,\Delta}$ , there  $J_{K,N}^{[m]} \triangleq \binom{(K+1)^2-1}{N}$  ways to place  $N$  tags in  $\mathcal{G}_{M,\Delta} \setminus \{\mathbf{u}_R\}$  if the ordering of how they are placed is not accounted. The calculation of a topology-independent average outage probability over all possible grid topologies requires an averaging over all  $J_{K,N}^{[m]}$  such topologies. Because  $J_{K,N}^{[m]}$  is enormous, especially for large  $K$ , the averaging in this work is applied through Monte-Carlo, i.e., for sufficient number of times repeat the following experiment: (a) sample uniformly a topology  $\mathcal{T}_L^{[m]}$  (each of them has probability  $1/J_{K,N}^{[m]}$ ), (b) calculate  $\Pr(\overline{\text{out}}_L^{[m]} | \mathcal{T}_L^{[m]}, \theta)$  (as well as the corresponding bound) for the sampled topology. Finally, the averaging is applied over the sampled topologies. The same reasoning can be applied to a bistatic system with  $L$  CEs and a single SDR reader, where  $J_{K,L,N}^{[b]} \triangleq \binom{K^2+2K-L}{N}$  random choices exist.

# Chapter 3

## Implementing a Bistatic Scatter Radio Network

In this chapter the implementation of a bistatic scatter radio network will be presented. In the beginning an overview of the network components will be presented, and then each component will be presented individually. Implementation details, and algorithms are presented for each component.

### 3.1 Network Components Overview

A scatter radio network consists of multiple digital scatter tags, multiple CEs and a reader. The CE is a typical Marconi embedded radio operating at the UHF band (866 – 868 MHz), and its main function is to transmit a constant wave, illuminating the tags. The CE's central frequency and the output power can be controlled via software. The digital scatter tags consist of a micro-controller unit (MCU), a SMA antenna connector, and a single RF transistor front-end. The incident CE's signal illuminates the tags, which scatter their information to the reader. On the receiving end a commodity software defined radio (SDR) is used for capturing the scattered signals at the UHF band, which is the European ISM band. The received signals are processed on a host PC by software. The signal processing is done on either MATLAB with custom scripts, or on the GNURadio framework, in Python and C++.

### 3.2 Scatter Tag Implementation

The most important component of the network is the scatter tag. The tag is responsible for sensing and transmitting the sensed data to the reader. In order to develop the tags in a more organised and independent manner, a modular architecture is utilized, and the tag is divided in three different boards:

- Scatter board
- Power board
- Sensor board

The scatter board is responsible for the communication and the sensor reading operations, the power board contains all the power sources and circuits, while the sensor board contains all the sensors, which are read by the scatter board.

### 3.2.1 Scatter Board

When constructing a WSN for precision agriculture, ultra-large scale deployments are a necessity. To achieve microclimate monitoring and environmental sensing in such a scale, ultra-low power and ultra-low cost sensor nodes are needed. The scatter radio technology achieves communication with a single transistor front-end, reducing the monetary and energy costs. The tag consist of an 8051 MCU, which is responsible for reading the outputs of the sensors connected to its input/output (I/O) pins, and transmit the read data to the reader. The MCU is connected to an RF transistor and communication is achieved by turning the transistor on and off.

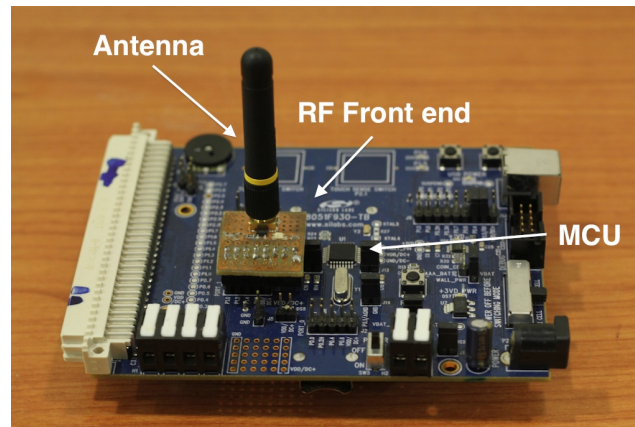


Figure 3.1: First semi-passive tag prototype. A commercial MCU development kit was used, with a custom made front end PCB.

The first prototype developed consists of an evaluation board from Silicon Laboratories, and a custom front-end printed circuit board, as depicted in Fig. 3.1. The particular MCU was chosen for two reasons: a) its ultra-low power consumption, and b) its comprehensive manual. The MCU is a low-power 8051 architecture unit, with C language program capabilities. It has two modes of operation, in one-cell mode it supports operation in the range 0.9 V to 1.8 V, and on dual-cell mode in the range 1.8 V to 3.6 V. Thus, in the beginning a 3 V coin cell battery was used for powering. Moreover, the MCU supports multiple clocking sources, such as the Low-Power Internal Oscillator, and an External Crystal Oscillator. For stability issues the external oscillator was used.

The second prototype developed is a custom made, one-layer PCB, combining the aforementioned MCU and the front-end. The PCB contains only the essential operating components needed by the tag, i.e. the MCU, the programmer, some I/O

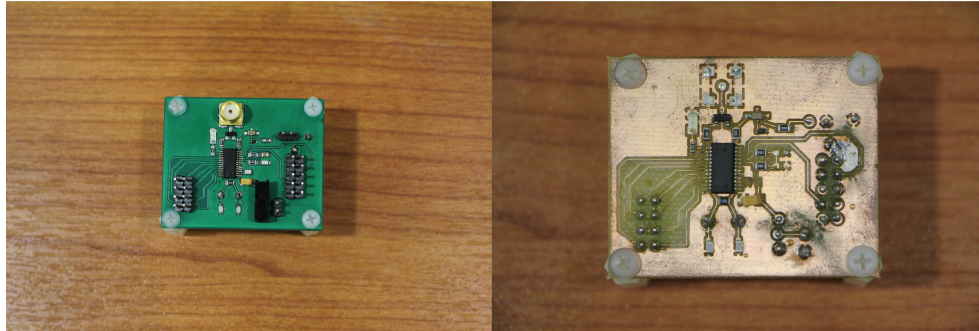


Figure 3.2: Second RF tag prototypes, where all the components are on the same board.

connections for sensors, the crystal oscillator, the RF transistor, and the antenna. The tag supports the basic operation of the network, sensing real-world data and transmitting them using scatter radio. This PCB also features a variable, voltage controlled load which could be controlled by the user. The variable load, can be used to change the transistor's switching loads resulting in better scattering. It has to be noted, that the design and the construction of the tags were done in-house in the Fabrication Laboratory of the Technical University of Crete. The constructed boards are depicted in Fig. 3.2 and the node is depicted in Fig. 3.4.

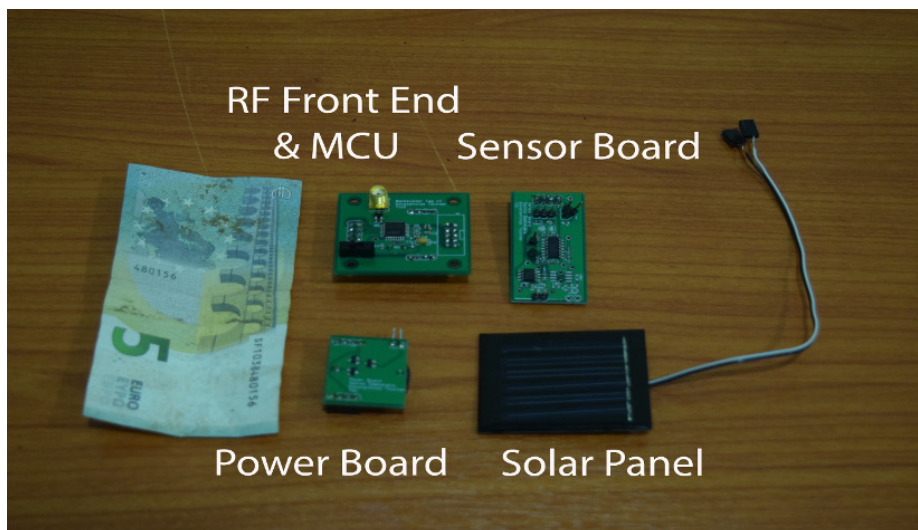


Figure 3.3: Final version of the scatter radio tag.

The final scatter board contains all the control and communication logic of the tag. Detailed schematics and layouts of the board can be found in appendix 6.1. The main goal of the development of the scatter board is to reduce the power consumption, in order to make the tag battery-less, and increase the number of nodes, in order to create an ultra-large scale network. The MCU used for the scatter board is an ultra-low power and low cost 8051 architecture unit. It supports many clocking sources, but the ones that are used are the external oscillator, and the low power internal oscillator.

Moreover, it supports three different modes of operation, active, idle, and sleep mode. On active mode the MCU is active and has the highest power consumption. In order to conserve power the MCU should be active the least time possible, which means that it should work in the highest possible clock for the least possible time. With the highest possible clock (25 MHz external oscillator) the scatter tag consumes 120 mA for almost 100 ms (this is the time the MCU needs to read one sensor and transmit the sensed value).



Figure 3.4: The scatter sensor node in the tomato casing.

When not transmitting, the MCU should operate in either idle, or sleep mode. On idle mode, the MCU stops working and all the internal registers and memory retain their data, while all the analog and digital peripherals remain active, and have to be disabled manually. From the idle mode the MCU can "wake" up by an interrupt or a reset. On this mode the MCU consumes almost 4 mA, but it is inefficient, since the MCU consumes the same power as a Marconi type sensor. Thus, the MCU should be placed in sleep mode. On sleep mode the internal 1.8 V regulator (VREG0) is switched off and the power supply of all on-chip RAM is switched to the VBAT pin (see Figure 14.1). Power to most digital logic on the chip is disconnected; only PMU0 and the SmarTClock (Smart Real Time Clock) remain powered. This is very important, because the SmarTClock is responsible for waking up the tag. Analog peripherals remain powered in two-cell mode and lose their supply in one-cell mode because the dc-dc converter is disabled. In two-cell mode, only the Comparators remain functional when the device enters Sleep Mode. All other analog peripherals (ADC0, IREF0, External Oscillator, etc.) should be disabled prior to entering Sleep

---

Mode. The tag consumes less than  $1 \mu\text{A}$ , while on sleep mode.

### Active Mode

The structure of the tag's code is build around the sleep mode. The MCU is configured to use the 25MHz external crystal oscillator while on active mode. During this mode, the ADC polls the sensors connected to the MCU's pins and gathers the data. The data are then translated from integers to binary digits and are encoded using a Reed-Muller encoder. The Reed Muller encoder is implemented on the 8-bit MCU and uses real-world data as inputs. The produced codewords are transmitted using B-FSK modulation implemented by the MCU. Each tag is assigned to a particular frequency channel, i.e., a particular frequency pair for bit 1 and 0. The frequencies are generated by the MCU using a simple bit-banking technique, and the data rate utilized is 1 kbps. The MCU can produce thirty (30) stable frequency pairs, and thus with FDM the maximum supported users are thirty (See section 3.2.1). It has to be noted that also 2 and 2.5 kbps data rates are supported, but the number of pairs reduces significantly, as the data rate increases (15 users for 2 kbps, 10 users for 2.5kbps).

### Sleep Mode

When the MCU is done with the sensing, and the transmission, it prepares for sleep mode, i.e., the clocking source of the MCU changes from the external oscillator to the low-power internal oscillator, and all the analog and digital peripherals are disabled. In must be noted that when the external oscillator is to be disabled, a very specific order of operations must be executed. First the clock multiplier should change to the desired value that will be used later by the low-power internal oscillator. Then the clocking source should change, and after the new clock is stable, only then, should the external oscillator be disabled; otherwise the MCU keeps restarting due to the Missing Clock Detector. Moreover, the external oscillator bias current should be switched off to truly enter sleep mode. When the MCU enters sleep mode, it is waken up by an interrupt sent by the SmarTClock. This clock can be configured to send an interrupt, at most, every two days, and thus the duty cycle can be very flexible.

This great feature is the solution to the scalability problem. If two or more tags are configured to use the same frequency pairs, because they use individual clocks and are not synchronised in any way, the probability of two or more tags, transmitting simultaneously is almost zero, since each tag uses the channel (communication medium) for 80 ms. Hence, many tags can use the same frequency pairs, and sleep for 4 – 5 minutes and then transmit their information. Using this pseudo-time division multiplexing (pseudo-TDM) scheme, increases the total number of tags from thirty to many hundreds. The pseudo code of the tag's operation is depicted in Algorithm

1.

---

**Algorithm 1** The pseudo-code of the tag's code.
 

---

```

1: Initialization:
2:   Port_Initialization()
3:   Clock_Initialization(25 MHz)
4:   ADC_Initialization()
5:   Timer_Initialization()
6:   SmartClock_Initialization(sleep_time)
7: while 1 do {loop for ever}
8:   Change_Clock_To_External_Clock(25 MHz)
9:   Enable_ADC&Timer()
10:  Measure_Sensor()
11:  Disable_ADC&Timer()
12:  Encoding()
13:  Transmit()
14:  Change_Clock_To_Low_Power_Clock(32 kHz)
15:  Sleep() { Wait sleep_time seconds for wake up Interrupt }
16: end while

```

---

### Frequency Division Multiplexing (FDM)

In WSNs several multiplexing protocols have been developed over the years. But most of them require the existence of the down-link (sync-to-node communication). In our case the down-link does not exist, since the tags are receiver-less. Hence, the only multiple access scheme that can be utilized is frequency division multiplexing (FDM). This scheme is commonly used in analog and digital television and also the combination of FDM and TDMA is used in worldwide cellular communications. In FDM the communication medium, is divided in a number of channels, one for each user, the scheme is depicted in Fig. 3.5. B-FSK is ideal for frequency division multiplexing (FDM) since each user is given a different pair of frequencies to communicate on. The implementation of the FDMA scheme is not trivial as many problems need to be solved. The first problem that has to be addressed is the communication bandwidth. Since non-coherent B-FSK is used, each user's signal requires bandwidth  $W = \frac{1}{T}$ , where  $T$  is the bit period. The communication rate determines the bandwidth each user needs and ultimately the total number of users that can communicate simultaneously.

Since the 3rd harmonic of the first frequency exists, the available bandwidth is shrunked to only  $3F_0 - F_0 = 2F_0$ ,  $F_0$  is the first frequency of the first tag. Thus,  $F_0$  must be carefully chosen. If  $F_0$  is too close to the carrier there is a possibility that the signal utilizing  $F_0$  will be "buried" by the carrier emitter's clatter. On the other hand, if  $F_0$  is too far, the receiver's bandwidth will be too large. This way the receiver absorbs more

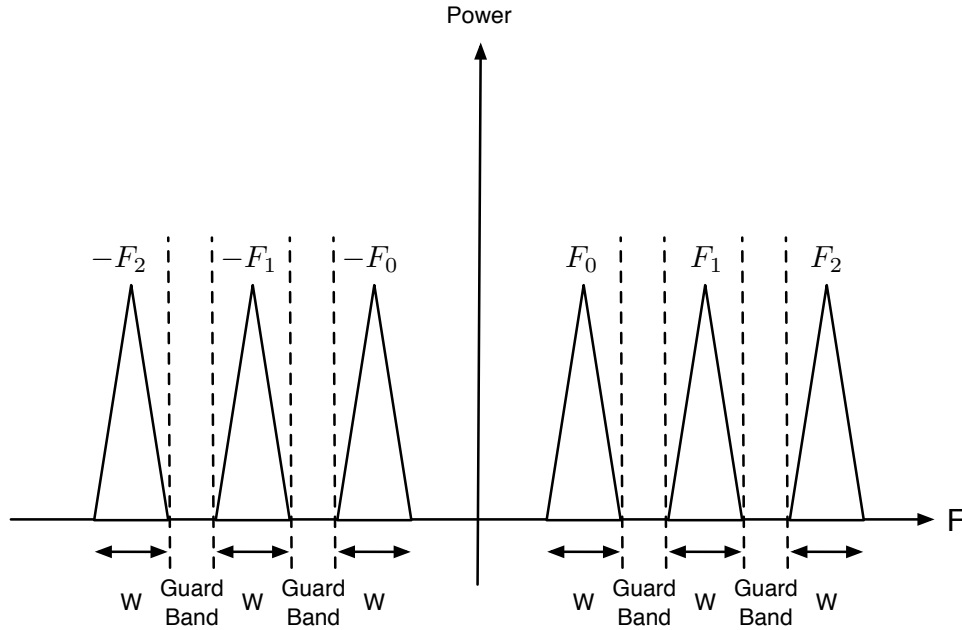


Figure 3.5: The FDM scheme used for the tags' MAC protocol.

noise which results in an increased noise floor (See Chap. 4.4), which decreases the receiver's performance. These trade-offs are really important. In this work,  $F_0$  is set at 100 kHz, thus the available bandwidth is  $W = 200$  kHz. Apart from the available bandwidth, another important aspect of the network that must be addressed is the guard bands. Each user uses a pair of frequencies and each transmitted signal uses  $W$  bandwidth. But it is not possible to create all frequencies that are apart from each other by  $W$  because of the utilized frequency generation scheme. Even if it were possible, it is bad practice not to leave some space between the users because even the slightest frequency offset at the tag would result to interference. Thus, guard bands must be introduced around each available communication frequency. But the guard band depends on the communication rate. In this work the communication rate is 1 kbps, hence each signal's bandwidth is  $W = 1$  kHz. The guard band is set at 500Hz from either side of the signal, summing to a total 1kHz guard band. Therefore, each user need 3kHz bandwidth, two for each frequency.

Theoretically, the aforementioned problems shrink the total number of users/ tags that can communicate simultaneously to only 66. But not all communication frequencies are available. Thus, the total number of users is 30. In Fig. 3.6 the spectrum of five users transmitting simultaneously is depicted.

### 3.2.2 Power Board

The main idea behind designing the power board is the use of ambient power sources. Ambient power can be harvested from the sun, the wind, from various RF signals

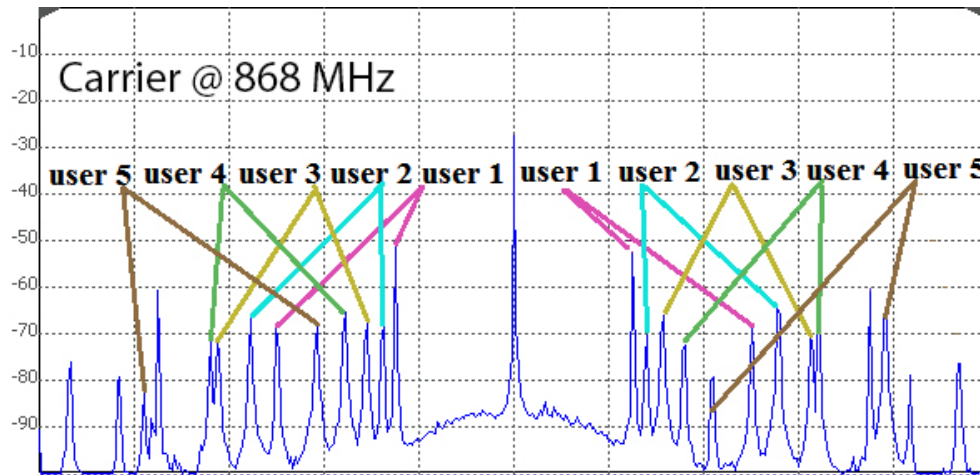


Figure 3.6: Spectrum of five tags transmitting simultaneously.

already present on the field. During the day the most efficient and accessible power source is solar energy. Small solar panels ( $2 \times 4$  cm) can provide enough energy for the tag to operate. But during the night, the tag needs to operate on another power source. Since, there are no ambient power sources powerful enough to power the tag, a battery or a battery-like component must be present.

The circuit connecting the two power sources, i.e., the solar panel, and the battery, must be able to change the source without disturbing the operation of the tag. Thus a simple OR gate was created with diodes to connect the two sources. During the day, when the solar panel provides more voltage than the battery, it is selected by the OR gate as the main power source. During the night the voltage of the solar panel drops, and the battery is selected as the power source. In order to guarantee that the voltage at the power pins of the MCU never changes, regardless of the power source, a voltage reference is added in front of the OR gate's output. The voltage reference causes the voltage of the power source to drop to a specific value (in our case 2 V), and does not allow any fluctuations. A schematic of the implemented power board can be found on Fig. 3.7 and a detailed schematic and layout are presented in appendix 6.2.

Since the tags consume  $1 \mu\text{A}$  in sleep mode, the battery can be removed from the power board. Instead a super capacitor can be used for night operation. The super capacitor will be charged during the day by the solar panel, and with the right duty cycle the tag can operate all night long by consuming the energy from the super capacitor. A schematic of the proposed power board can be found on Fig. 3.8

### 3.2.3 Sensor Board

The scatter network is designed for agricultural applications, and microclimate monitoring. Thus, the tags should support a vast range of sensors. The sensor board provides an easy way of developing and testing different sensors, without changing

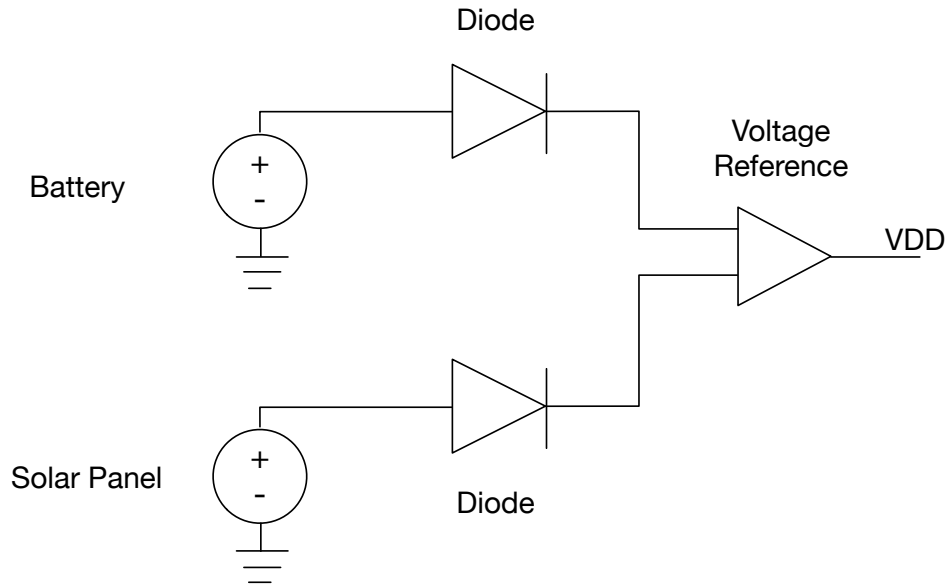


Figure 3.7: The schematic of the power board. A simple OR function between two power sources.

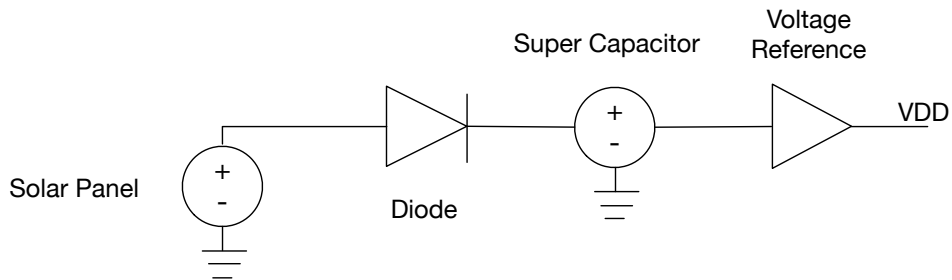


Figure 3.8: The schematic of the power board. A simple OR function between two power sources.

the communication and power parts of the tag. Each tag can read up to 6 sensors, which are powered by the tag. The sensed information can come in the form of either voltage measurements, or frequency measurements. This means that either the MCU's ADC, or a simple zero-crossing algorithm can be used to read the sensors, depending on the output. The reading methods are all implemented on the MCU.

In the network deployment, constructed as a proof-of-concept demonstration, the sensor board contained five sensors, i.e., a resistive temperature sensor, a soil moisture and an air humidity sensor, a photodiode, and a plant ECG sensor. These circuits were constructed and tested separately and then were integrated on a single board. A detailed schematic and layout will be presented in appendix 6.3.

### 3.3 Carrier Emitter Network - Cellular Architecture

The carrier emitters are the illuminators of the scatter radio network. The CEs are monolithic embedded radios operating in the European UHF band (866 – 868 MHz), and are very powerful tools. They support the transmission of a constant wave signal at the UHF frequency, with at most 13 dBm ( $\sim 20$  mW) power.

In order to cover a huge geographical area, multiple carrier emitters must be utilized. Around each carrier emitter a cell can be created, illuminating multiple tags (Fig. 3.9). In every cell the tags must have different frequency pairs, and IDs, but in different cell there can be frequency reuse, i.e., the frequency pairs of the tags can be shared in different cells. This is done only if one CE illuminates the tags during each time frame. To achieve that the CEs must have a medium access control (MAC) protocol. Since the CEs are embedded radios, a simple time division multiple access (TDMA) protocol can be implemented.

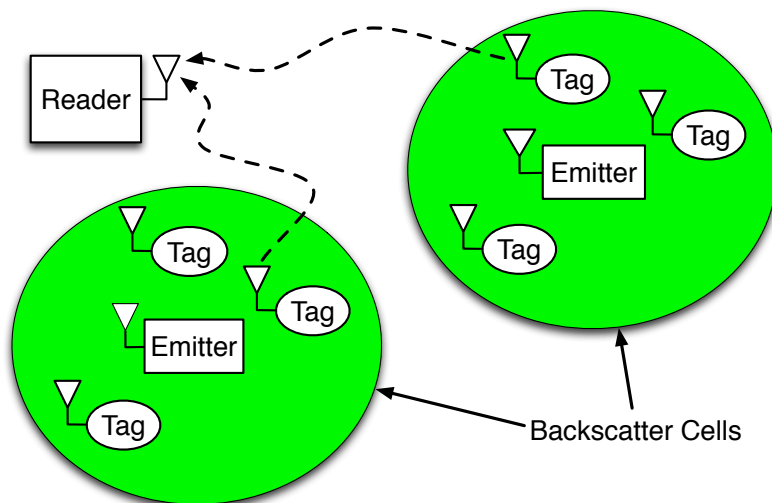


Figure 3.9: Scatter radio field with sensors/RF tags. Multiple carrier emitters are placed in the field to illuminate tags, along with a centralized receiver/reader.

The TDMA scheme is implemented using the Silicon Laboratories libraries. Each CE is given an ID number, which is used to determine the carrier wave (CW) transmission order. Since the order is predetermined, the CE with ID 1 broadcasts that it is now transmitting, and every other CE in the network waits until an other broadcast is transmitted, stating that the CW transmission is over. Then the CE with ID 2 broadcasts that it is now transmitting, and so on. With this simple scheme the frequency reuse across different cells is achieved.

## 3.4 Software Defined Radio Reader

The reader is responsible for the reception and processing of all the scattered signals. The SDR reader consists of a radio frequency (RF) front-end tuned in the UHF band and fast I/Q analog-to-digital converters (ADCs). The RF front-end captures the signals in the UHF band and use a demodulation chain to bring the signals to the baseband. The output is then sampled by the ADCs and is transferred, via Ethernet, to the host PC. The host is responsible for all the heavy signal processing work, which is either done on MATLAB or on GNURadio. The custom MATLAB scripts provide great flexibility, as the user can develop custom receivers for different modulation and coding schemes really fast and efficiently. The main drawback of this receiver development method is its linearity. In a network multiple tags transmit simultaneously (or almost simultaneously) and MATLAB scripts run the receiver code serially for each tag in the network, regardless of that tag's signal being received. The GNURadio framework provides a more systematic approach to the receiver development. The framework consists of many pre-made blocks for all the receiver chain, e.g., filtering, CFO estimation, channel estimation, detection. These blocks are made by the GNU community and are maintained by them, but in many cases these blocks are insufficient. Especially in the scatter radio communications using these blocks alone can reduce the performance by 50%. In this type of scenarios, the GNURadio framework offers a tool called `gr-modtool`. This tool allows users to develop their own custom blocks and write the block's code in either Python or C++. For network development, the GNURadio framework is preferred because of the high speed it provides. The receivers are executed in C++, i.e., a programming language with one of the faster implemented compilers, and do not require an interpreter (MATLAB uses a JAVA interpreter), which slows the things down significantly. Moreover, GNURadio processes the ADC samples as a stream, while in the MATLAB implementation the data are processed in packets, and while a packet is processed the rest samples wait in a queue.

### 3.4.1 MATLAB Implementation

MATLAB provides a framework, where receivers can be implemented very quickly. The ADC samples are transferred from GNURadio to a FIFO, which can be opened in the MATLAB script. The signal processing chain is implemented in custom scripts. For scatter B-FSK, which is presented in section 2.1.2, the signal processing chain is presented in Fig. 3.10. For multiple tag reception, multiple chains must be created, and MATLAB does not support parallel processing of the chains. Thus, these scripts are very slow, decoding 1 tag per second.

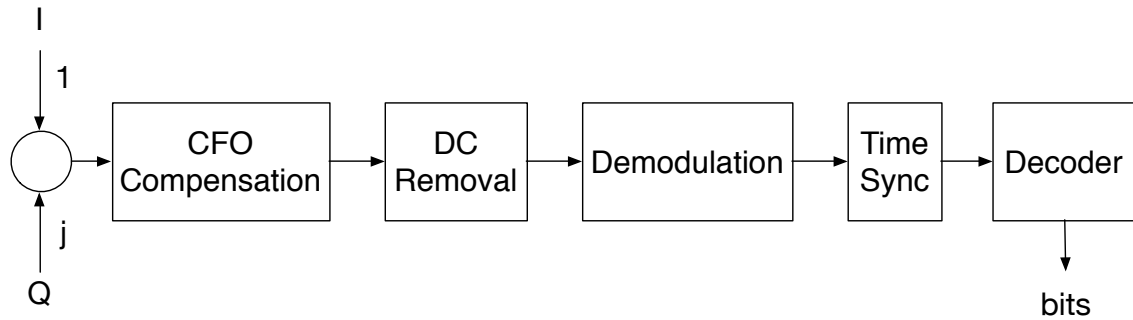


Figure 3.10: Simulation setup 2. The emitter is placed on the edge of the field and the tag-of-interest is moved away from the emitter, while the two interferers are closer to the emitter and the reader.

### 3.4.2 GNURadio Implementation

GNURadio is the main framework, with which the SDR receivers operate. The framework consists of many pre-made blocks for all the receiver chain, e.g., filtering, CFO estimation, channel estimation, detection. These blocks are made by the GNU community and are maintained by them, but in many cases these blocks are insufficient. Thus, new blocks can be created, serving our needs using the `gr-modtool`. The implementation of the signal processing chain of the scatter radio network is done in Python, which is used to connect all the C++ blocks, and in C++ which is the main language of the signal processing blocks.

In order to implement the chain two blocks need to be created in C++, the block responsible for the time synchronisation, and the block for the DC removal. Moreover, a frequency lock loop (FLL) needs to be created for the CFO estimation and correction. The FLL was created by combining several pre-existing GNURadio blocks, like the FFT block, the magnitude-square block and the x-lating filter block (a block that multiplies two signals on real-time). The signal processing chain implemented in the GNURadio receiver is shown on Fig. 3.11.

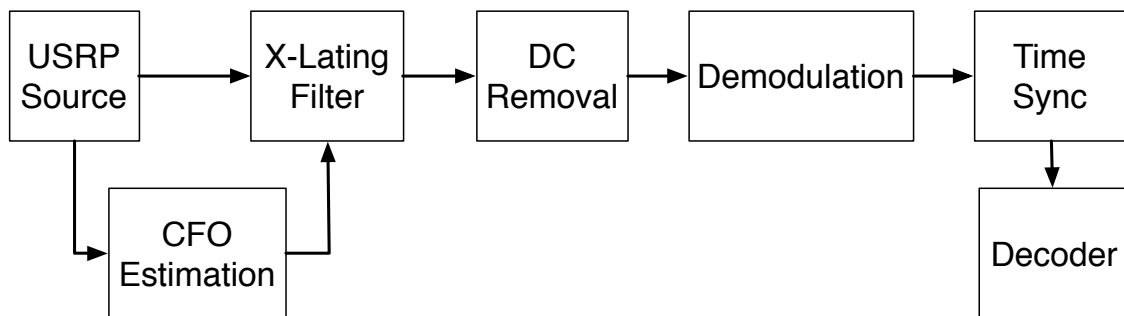


Figure 3.11: Simulation setup 2. The emitter is placed on the edge of the field and the tag-of-interest is moved away from the emitter, while the two interferers are closer to the emitter and the reader.

Table 4.1: Simulation Parameters		
$N_0 _{\text{dB}} = -174 + \text{NF} \text{ (dBm/Hz)}$	$\mathbf{h}_{T_n} = 1 \text{ (m)}, \forall n$	$\lambda = \frac{1}{3} \text{ (m)}$
$\text{NF} = 8 \text{ (dB)}$	$\mathbf{h}_R = 1.7 \text{ (m)}$	$\mathbf{s}_n = 0.1, \forall n$
$ \Gamma_{n,0} - \Gamma_{n,1}  = 2, \forall n$	$\mathbf{h}_{C_l} = 1.7 \text{ (m)}, \forall l$	$\mathbf{G} = 2.15 \text{ (dBi)}$

## Chapter 4

# Simulation and Experimental Results

### 4.1 Numerical Results

From Eqs. (2.37) and (2.31) it is already apparent that the bistatic system offers diversity order at least 1, while monostatic system only  $\frac{1}{2}$ . It is emphasized that the diversity order of bistatic system equals the one of classic point-to-point Marconi radio Rayleigh fading system with single antenna [22].

Fig. 4.1 offers BER performance as function of SNR for the two scatter radio architectures, assuming  $N = 1$  tag/sensor,  $L = 1$  slot and common  $\text{SNR} = \text{SNR}_{1,1}^{[b]} = \text{SNR}_1^{[m]}$  (resulting to monostatic reader transmission power  $P_R$  and bistatic carrier emitter power  $P_{C_1}$  related according to  $P_R = \frac{L_{C_1, T_1} P_{C_1}}{L_{T_1, R} 2}$ ). Eq. (2.27) and [13, Eq. (27)] are used for the monostatic and the bistatic architectures, respectively. It can be seen that the bistatic point-to-point system outperforms the monostatic one and high-SNR slope is clearly different, as expected. It can be also seen that their performance gap increases with increasing SNR.

For a large-scale network the impact of  $\theta$ ,  $N$ , SDR reader and CE transmission power in topology-independent average outage probability is investigated for both monostatic and bistatic architectures. Average outage probability calculation utilizes 1000 randomly chosen topologies, as explained in Section 2.4.1; for each topology,  $\Pr(\overline{\text{out}}_L^{[m]} | \mathcal{T}_L^{[m]}, \theta)$  and  $\Pr(\overline{\text{out}}_L^{[b]} | \mathcal{T}_{L,N}^{[b]}, \theta)$  are calculated using 2000 Monte Carlo experiments, as well as their corresponding upper bounds. The comparison of the two schemes is carried out in the  $\mathcal{G}_{160,5}$  grid network (i.e.,  $M = 160$  and  $\Delta = 5$ ). The SDR reader is placed at the middle of the topology in order to maximize the coverage, i.e.,  $\mathbf{u}_R = [80 \ 80]^\top$ , while for bistatic architecture with  $L = 4$ , CEs' positions are given by  $\{\mathbf{u}_{C_l}\}_{l=1}^4 = \{[40 \ 40]^\top, [120 \ 120]^\top, [120 \ 40]^\top, [40 \ 120]^\top\}$ . In Fig. 4.2-Left (-Right) the network setup of monostatic (bistatic) setup is depicted.

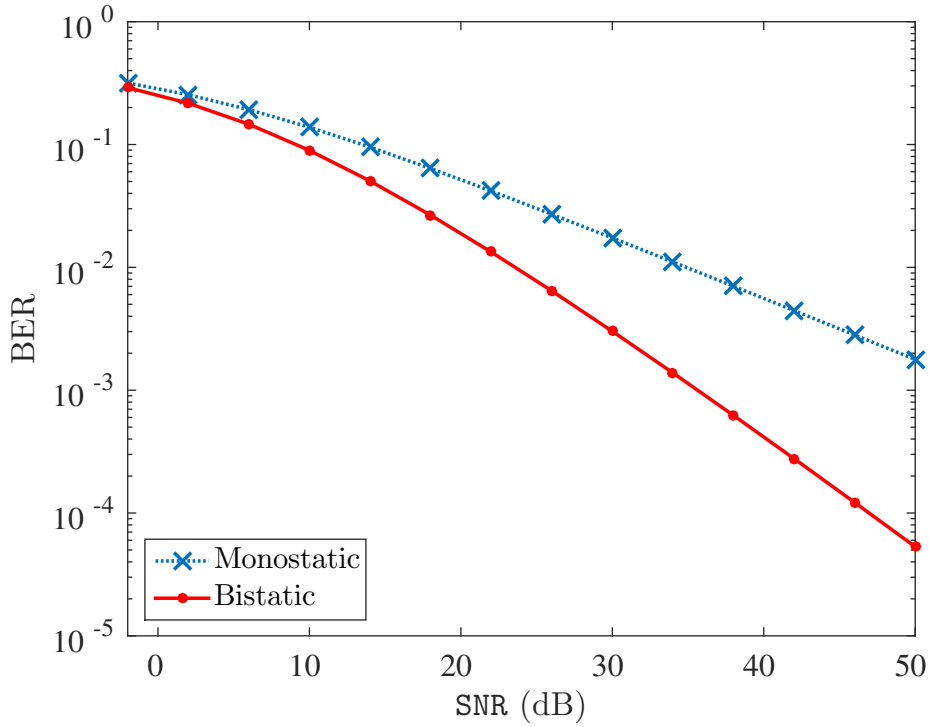


Figure 4.1: BER performance under ML coherent detection for monostatic and bistatic architecture.

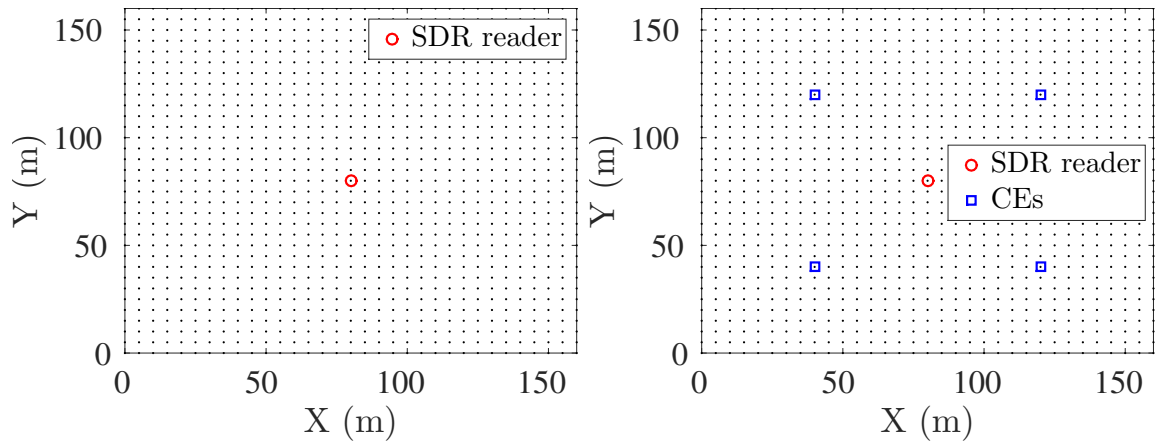


Figure 4.2: Network setup: monostatic (left) and bistatic (right) with 4 carrier emitters (CEs). Grid points (dots) are possible tag/sensor locations.

Each tag backscatters information using bit period  $T = 1$  ms (1 Kbps). Table 4.2 offers the simulation parameters. In addition,  $\varepsilon_{n,j} = 2\pi T$  for all  $n, j \in \mathcal{N}$  with  $n \neq j$ , and each tag  $n$  utilizes the following pair of frequencies (that satisfy the orthogonality criteria of Section II, Eq. (2.17):  $F_{n,0} = (0.1 + n F_{\text{sp}})$  MHz and  $F_{n,1} = (0.1 + n F_{\text{sp}} + F_{\text{sp}}/5)$  MHz with  $F_{\text{sp}} = 0.01$  MHz (as well as their negative counterparts), offering from Eq. (2.40),  $\rho_{nj} = \rho_{jn} = \frac{25}{[2\pi T (5|n-j|-1) F_{\text{sp}}]^2}$ .

Fig. 4.3 illustrates the topology-independent average outage probability (as well as the corresponding upper bounds) for monostatic and bistatic architectures as a

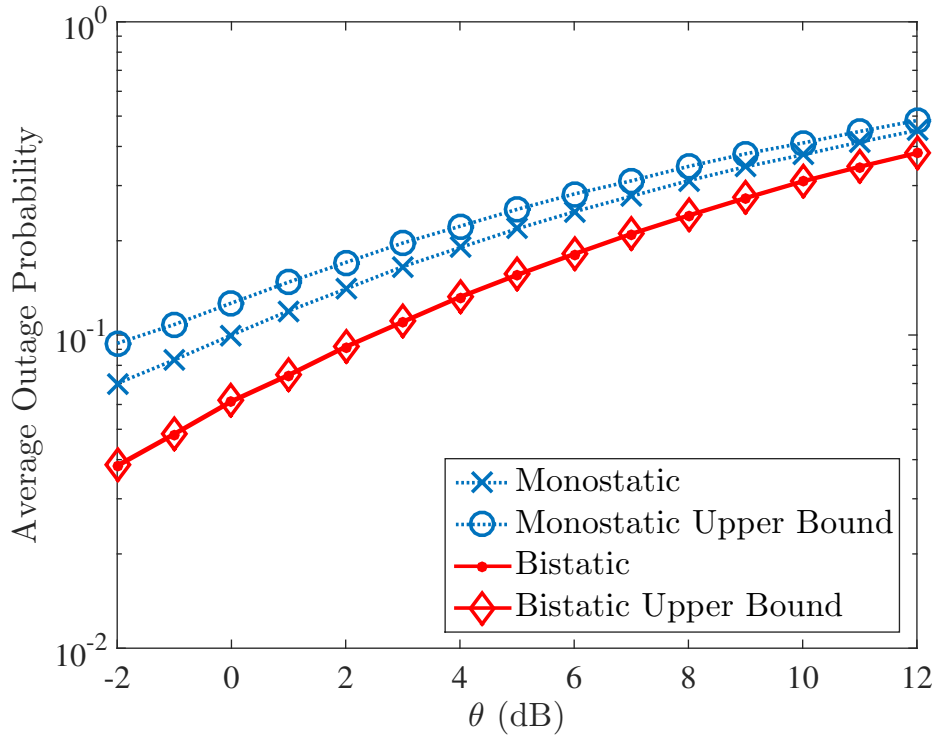


Figure 4.3: Tag topology-independent, average outage probability as a function of threshold  $\theta$  for monostatic and bistatic systems in setup of Fig. 4.2.

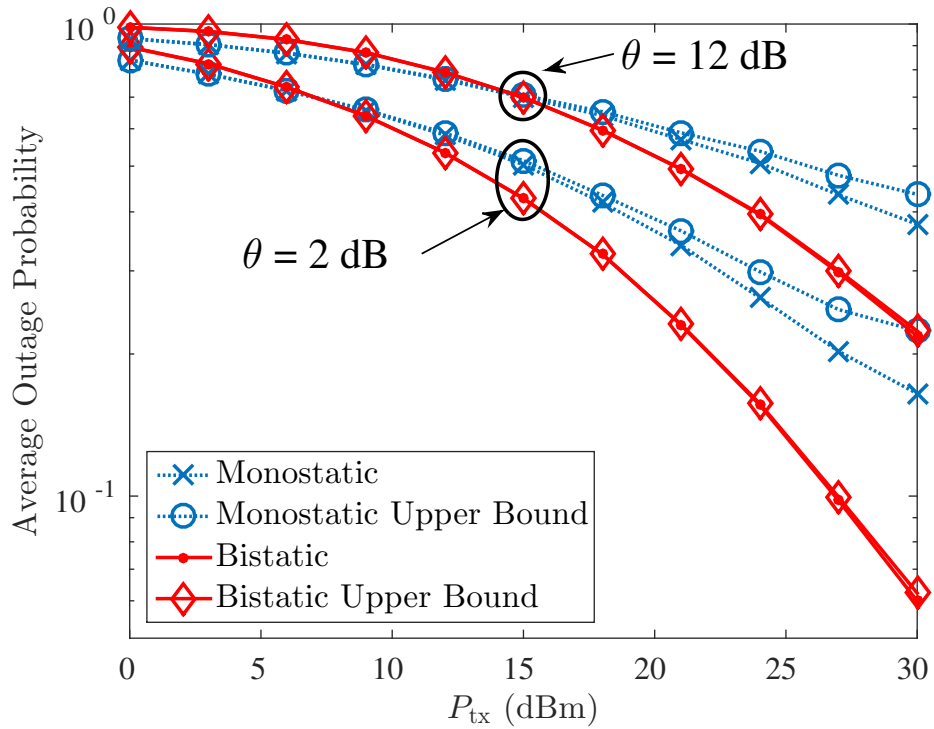


Figure 4.4: Tag topology-independent, average outage probability as a function of transmission power  $P_{tx} = P_R = P_{C_i}$  for monostatic and bistatic systems in setup of Fig. 4.2.

function of threshold  $\theta$ , for  $N = 100$  tags and equal transmission power per slot for both systems, i.e.,  $P_R = P_{C_l} = 20$  (dBm),  $\forall l$ . It is noted that the specific monostatic network setup (Fig. 4.2-Left) is the most appropriate among all possible choices of  $\mathcal{G}_{160,5}$  in terms of coverage, since the SDR reader is located in the middle of the grid. Fig. 4.3 shows that for  $\theta \in [2, 10]$ , the bistatic architecture outperforms the monostatic, with a performance gap of 2dB. The gap between the performance of two systems increases as threshold  $\theta$  decreases. It can be also remarked that for the specific setup of bistatic and monostatic grid topologies, the proposed bounds are quite tight, especially for the bistatic system, where the difference among bound and exact curve is negligibly small. From the above observations, the bistatic architecture offers more reliable reception compared to monostatic, or equivalently, larger network coverage, for a broad range of reception thresholds  $\theta$ .

Fig. 4.4 offers tag topology-independent outage probability for both monostatic and bistatic architectures, as a function of transmission power  $P_{tx}$  assuming  $N = 100$  tags. Results for  $\theta = 2$  and  $\theta = 12$  are illustrated and as expected, smaller  $\theta$  offers better performance for both schemes. It is noted that for small values of  $P_{tx}$  monostatic system offers smaller outage; however, at that low  $P_{tx}$  regime, the outage probability values are quite large, in the order of 70% percent. As  $P_{tx}$  increases, the bistatic architecture outperforms the monostatic and the performance gap among them also increases. It can be deduced that for the specific network setup, tag topology-independent outage less than 10% requires the bistatic architecture with CE transmission power  $P_{tx} \geq 27$ dBm and  $\theta = 2$ .

Finally, Fig. 4.5 studies the impact of number of tags  $N$  in average outage probability for monostatic and bistatic systems, assuming equal transmission power per slot, i.e.,  $P_R = P_{C_l} = 20$  (dBm),  $\forall l$ . It can be seen that as the number of tags increases, monostatic system's tag topology-independent average outage probability tends to increase slowly, in sharp contrast to bistatic system, where average outage probability remains unaffected. This implies that in the monostatic architecture with large number of tags, there exist tag topologies which are significantly affected from interference or weak SNR; on the contrary, the bistatic architecture is flexible enough, permitting several tags to operate concurrently, with outage performance less sensitive to the number of tags and smaller, outperforming the monostatic architecture, for the specific setup.

Taking into account all the above, it is clear that the bistatic architecture offers higher reliability or equivalently better field coverage for scatter radio WSNs.

Taking into account that for each tag only two interferers exist, several network topologies with three tags (the tag-of-interest and two interferers) were simulated. The parameters used in the simulations are shown at Table 4.2. In all tested topologies the reader is placed at the middle of the test area, which is an  $100 \times 100$  m<sup>2</sup> grid,

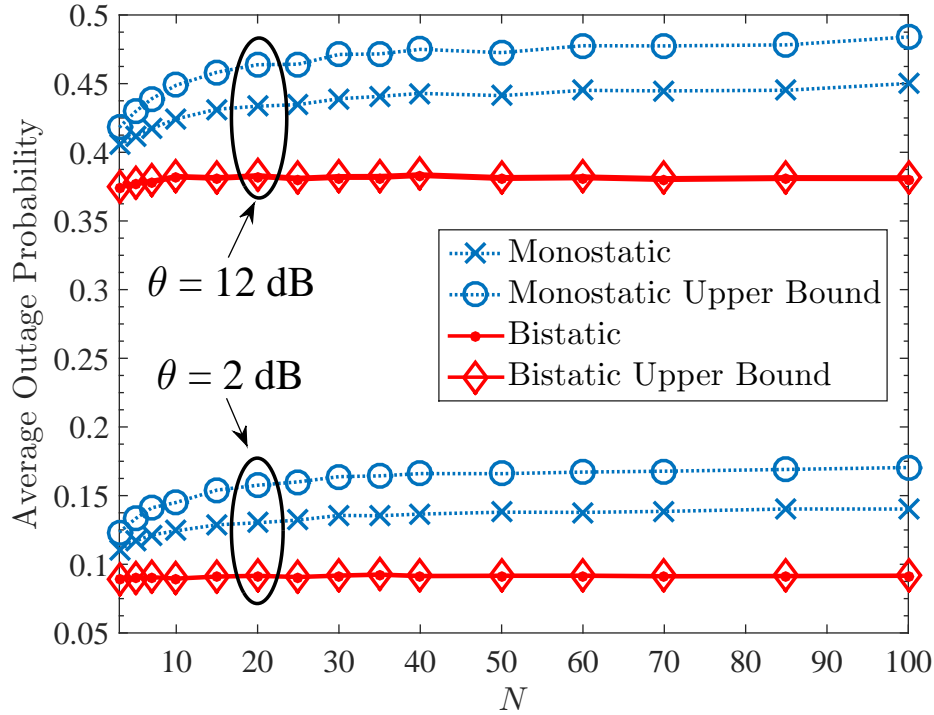


Figure 4.5: Tag topology-independent, average outage probability as a function of  $N$  (number of tags), for monostatic and bistatic systems in setup of Fig. 4.2.

with 1 m resolution. In order to determine threshold  $\Theta$ , we fix the outage probability of the monostatic architecture to 1% and work without interferers. Therefore  $\Theta$  is calculated as follows using (2.24) and (2.45):

$$\begin{aligned} \Pr\left(\overline{\text{out}}_L^{[m]} | \mathcal{T}_N^{[m]}, \theta\right) &= F_{g_{i,n}^{[m]}}\left(\frac{2\theta}{\text{SNR}_n^{[m]}}\right) \Rightarrow \\ \Rightarrow F_{g_{i,n}^{[m]}}\left(\frac{2\theta}{\text{SNR}_n^{[m]}}\right) &= y \Rightarrow F_{g_{i,n}^{[m]}}^{-1}(y) = \frac{2\theta}{\text{SNR}_n^{[m]}} \end{aligned} \quad (4.1)$$

We calculate the inverse of (2.41):

$$F_{g_{i,n}^{[m]}}^{-1}(y) = \ln^2(1 - y), \quad (4.2)$$

and substitute in Eq. (4.1) in order to get outage probability of 1%:

$$\ln^2(1 - 1\%) = \frac{2\theta}{\text{SNR}_n^{[m]}} \Rightarrow \theta = \frac{\text{SNR}_n^{[m]} \ln^2(0.99)}{2} \quad (4.3)$$

For example, for given  $\text{SNR} = 20$  dB, we calculate the parameter  $\Theta \approx 1$ . In Fig. 4.1 the probability of outage without interferers, for  $\Theta$  corresponding to  $\text{SNR} = 10$  dB is depicted (the same  $\Theta$  is used thereafter). Literally, this figure shows the probability of deep fade in the two architectures and it can be deduced that the monostatic

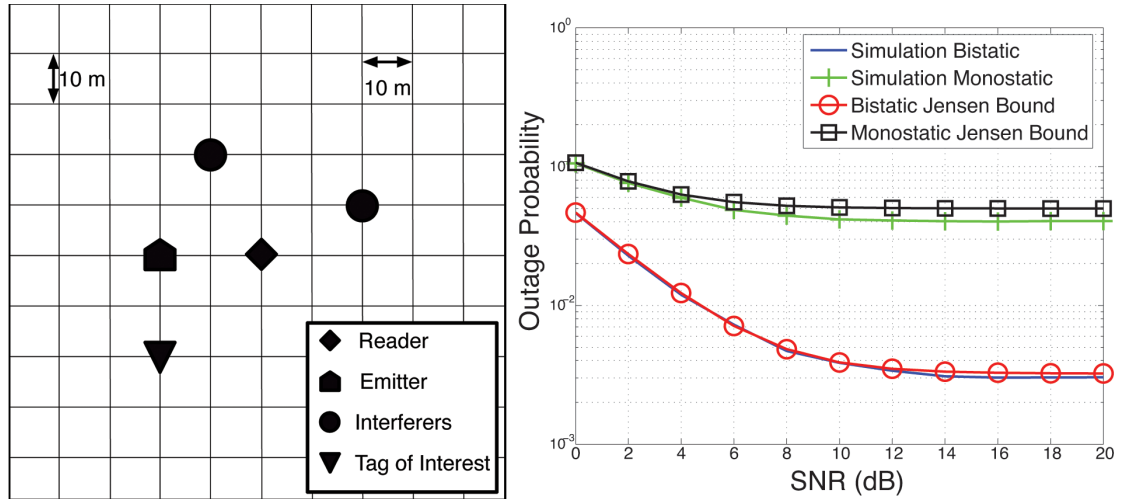


Figure 4.6: Simulation setup 1. The tags and the emitter are close to the reader, resulting to good performance for both architectures.

architecture has two orders of magnitude bigger probability of deep fade than the bistatic architecture.

In Fig. 4.6-Left, the first setup is depicted; the distances between the components are small and thus, the probability of outage is small, as shown in Fig. 4.6-Right. The bistatic architecture achieves better performance, even better than the desired 1% at 10 dB SNR. Moreover, in setup 2, shown in Fig. 4.7-Left, the emitter is placed at one corner of the test area and the interfering tags are placed between the reader and the emitter, while the tag-of-interest is placed further away from the emitter. This topology favors the monostatic architecture because the distance between the reader and the tag is much smaller than the distance between the tag and the emitter. From Fig. 4.7-Right can be deduced that the bistatic architecture has better performance than the monostatic one, even though the performance gap closes due to the large distance between the carrier emitter and the tag-of-interest. In the final scenario, the emitter is placed at the edge of the field and the tag-of-interest at the opposite edge, thus the emitter-to-tag distance is maximized. The two interferers are placed in-between the emitter and the reader, as shown in Fig. 4.8-Left. One could expect that the monostatic architecture would have better performance, but the results of Fig. 4.8-Right suggest otherwise. Again the bistatic architecture has better probability of outage than the monostatic. In this case the derived bounds are not as exact as in the other two scenarios, since the tag-of-interest-to-emitter distance is large and the interference is strong. It is clear that the bistatic architecture offers improved coverage and performance, in contrast to the monostatic one.

Table 4.2: Parameters for Numerical Results

$G_{\text{Tx}} = G_{\text{Rx}} = 2.15$ dBi	$h_{\text{T}} = 2$ m	$\lambda = \frac{1}{3}$ m
$R = 1$ Kbps	$h_{\text{R}} = 2$ m	
$\eta = -10$ dB	$h_{\text{C}} = 2$ m	

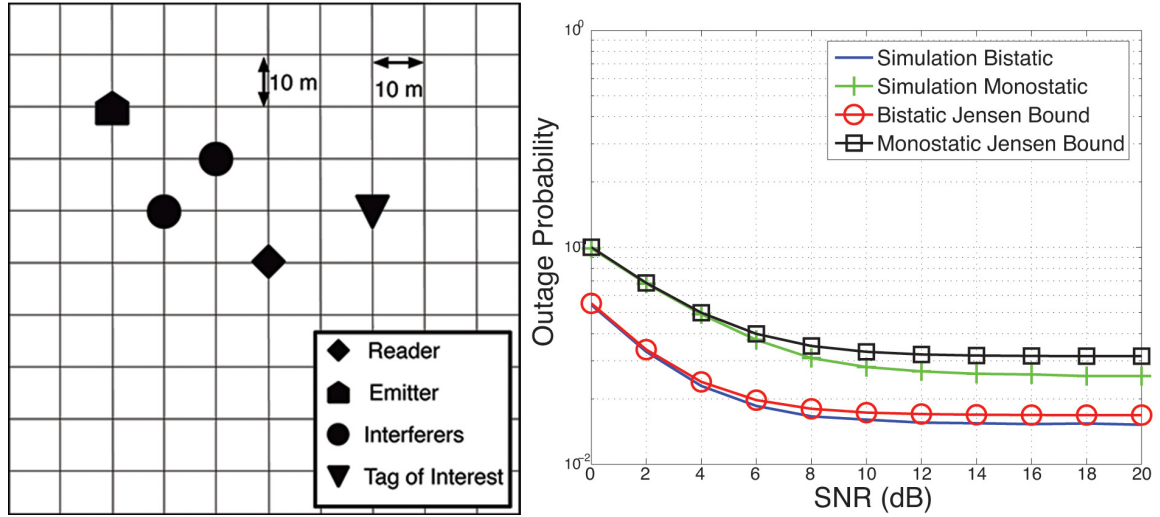


Figure 4.7: Simulation setup 2. The emitter is placed on the edge of the field and the tag-of-interest is moved away from the emitter, while the two interferers are closer to the emitter and the reader.

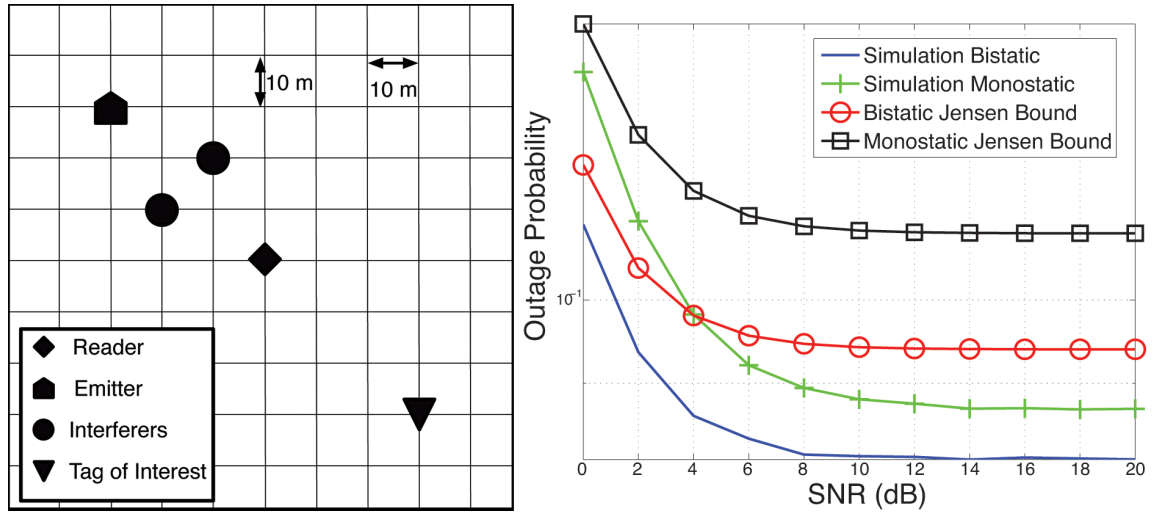


Figure 4.8: Simulation setup 3. The distance between the emitter and the tag-of-interest is almost maximum.

## 4.2 Experimental Results

### 4.2.1 Coverage

In order to validate the numerical results an experimental campaign was conducted, comparing the coverage of the monostatic and the bistatic architecture. The experimental setup consisted of an SDR reader connected to a host PC, a CE and three tags. The tags were transmitting a fixed data word, using BFSK modulation in different subcarrier frequencies, at 1Kbps data rate. Moreover, the tags employed a 1/2 rate Reed-Muller channel code for error correction. The CE transmitted power was set 13dBm, at 868MHz. Furthermore, in order to simulate a monostatic reader, the SDR reader and the CE were placed on the opposite sides of a metal box. This structure provided good isolation ( $\sim 15$ dB) between the transmit and the receive antennas, without the use of a circulator. The monostatic setup used for the experimental campaign is depicted in Fig. 4.9.

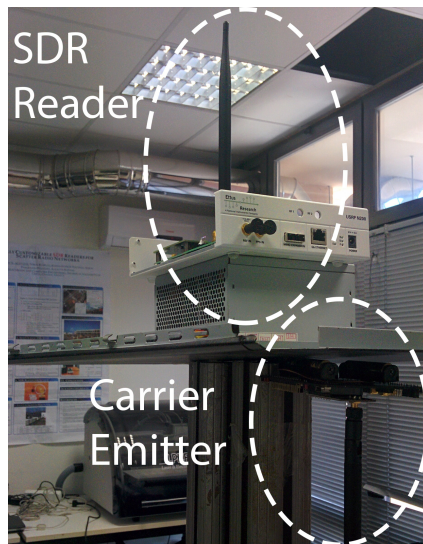


Figure 4.9: The custom monostatic reader used for the experimental campaign. The reader is on the top side of a metal box, while the CE is on the bottom side.

The campaign consisted of two stages. In the first stage the maximum achieved ranges of the tag-to-SDR reader links were calculated. The metric used to find the maximum range was the tag's bit-error-rate at the receiver; the maximum allowed bit-error-rate was 5%. The bistatic architecture achieved tag-to-SDR reader ranges over 140m, with tag-to-CE ranges being in the order of tenths of meters. The achieved ranges of the monostatic setup were one order of magnitude smaller than the bistatic, with the maximum tag-to-SDR reader range being  $\sim 15$ m.

In the second stage the coverage of a field of total area 3500m<sup>2</sup> was examined. For the bistatic architecture two network topologies were deployed, one with three CEs and one with four. In the first topology (shown in Fig. 4.10) the SDR reader was

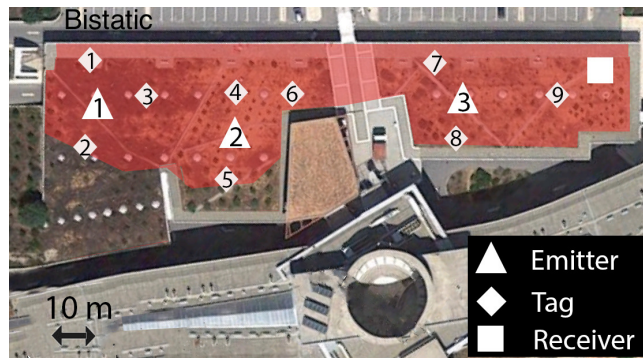


Figure 4.10: First bistatic setup deployed. The reader was placed at the corner, while the CEs were placed around the field to maximize the coverage of the tags.

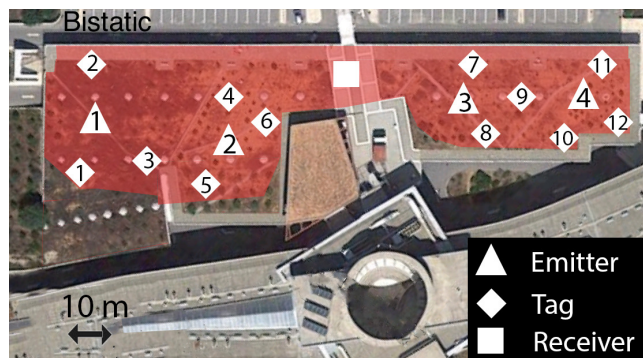


Figure 4.11: Second bistatic setup deployed. In this case the reader was deployed at the center of the field while the emitters were placed in almost antipodal positions to maximize the tags' coverage. Because the tag-to-SDR reader distances were smaller, the coverage increased.

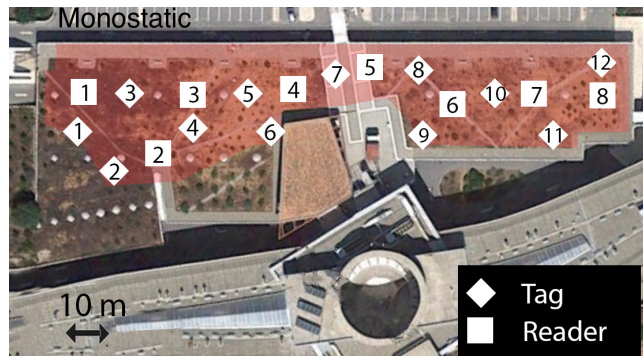


Figure 4.12: Monostatic setup deployed. In this case the readers were deployed every  $\sim 20$  m, with the tags around them.

placed in one corner of the field, maximizing the tag-to-SDR reader distance, while the CEs were placed around the field, in order to maximize the coverage. In the second topology the reader was placed in the center of the field, as shown in Fig. 4.11. In this case in order to cover the whole field four emitters were needed. For the monostatic architecture, multiple readers/CEs were deployed. Since the monostatic architecture's ranges are shorter a total of eight readers were used, as shown in Fig. 4.12.

The experimental campaign showed that both the monostatic and the bistatic setups can cover the same area, but the drawbacks of the monostatic setup were clear. The monetary costs of the monostatic system are significantly greater than the bistatic's, since every twenty meters a new SDR reader along with a host PC must be deployed. The bistatic architecture, with its flexible topologies and greater ranges provided coverage of the same area with only a single SDR reader and multiple CEs, which can come in a form of a synthesiser and an amplifier connected to an antenna.



Figure 4.13: The scatter sensor network deployed on the garden. The tomatoes are the tags.

### 4.2.2 Sensing

In Fig. 4.14 the temperature and soil moisture reported data of two tags are depicted. The tags were deployed on the garden of Technical University of Crete and operated by the solar panel during the day and by battery during the night (Fig. 4.13, Fig.3.4). The tags were deployed for 14 hours. In Fig. 4.14-Left are shown the soil moisture sensor measurements. The moisture of the ground was around 13 – 15% until midday, when the plant was irrigated, when the measurements rose to 55% and 30%. Moreover in Fig. 4.14-Right the measured temperature is depicted. Sensor 2 was placed directly under the sun and thus the reported temperature is much higher than sensor 1 which was protected from the sun.

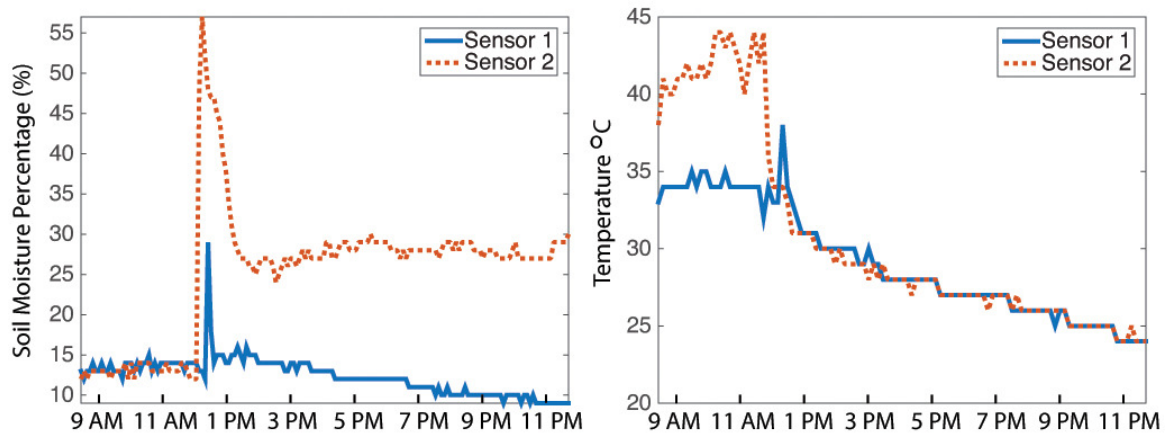


Figure 4.14: Left: Soil moisture measurements, Right: Temperature measurements

# Chapter 5

## Conclusion & Future Work

### 5.1 Conclusion

This work aimed at low-cost environmental sensing with scatter radio technology, mainly for agricultural applications. Ultra-low cost, low power and high network density were the highest design priorities (and constraints). The bistatic scatter radio system was presented, which can be utilized to build large scale low-cost and low-power sensor networks with extended field coverage. The individual modules of the system were presented: carrier emitter and tag prototypes, along with a software-defined reader. The complete signal model was derived for both the bistatic and the monostatic architectures. The two architectures were compared in terms of bit error rate for maximum likelihood detection for the single user case, where the diversity order of each architecture was derived, and outage probability for the multiple user case, where tight bounds were derived. It was clearly shown that the bistatic architecture surpasses the monostatic one in terms of coverage and performance. Taking this fact into account, a bistatic digital scatter WSN was constructed. The prototype tags use binary FSK and FDM to communicate with the reader and report real-time data sensed by a sensor board. The scatter board consumes less than  $1 \mu\text{A}$  on sleep mode and operates only on a small solar panel. With the use of “sleep” mode the maximum amount of tags supported by the network is greatly extended to over 300 depending on the duty cycle. The network was tested in two deployments, where it reported the soil moisture, temperature and luminosity values of the field.

---

## 5.2 Future Work

This work is a large step towards the implementation of ultra-large scale scatter sensor networks. With the use of the bistatic architecture, it is possible to deploy large networks with receiver-less tags.

The total network tags is connected with the tags' duty cycle. In order to extend the total number of users, a simple receiver could be implemented on the tags, in the form of a single diode and a capacitor. This could allow the implementation of simple on-off-keying (OOK) modulation on the emitters, in order to implement proper TDMA protocols. This could limit the communication range between the tag and the reader, but since the emitters are close to the tags with high probability, the range reduction would not be significant.

The tag's front-end should be redesigned, in order to maximize  $|\Gamma_1 - \Gamma_0|$ . By maximizing this quantity the tag-reader communication range would greatly increase. This requires an extensive microwave analysis and design of the front-end, along with an extensive characterization of the RF transistors used for the front-end.

Moreover, the tag's power board should be developed to allow powering only by ambient sources. The new generation power board should utilize multi-modal powering techniques, combining solar power, RF harvesting, and plant energy. This will reduce the tag's cost and will create a truly battery-less and energy efficient tag.

Finally, the GNURadio receivers should be further developed, taking into account the number of tags transmitting at each time instance. As it stands, the receiver tries to decode each tag, even if it does not transmit at the moment. The receiver should be more clever and try to find which tags are trying to communicate with it, and only run the signal processing process for the specific tags. This would reduce the delay at the receiver and increase the network's efficiency.

Hopefully, the expansion of this work will enable ultra low-cost and large-scale environmental sensing, which was previously unfeasible with existing technologies, both due to limiting cost and relatively high energy demands.

# Chapter 6

## Appendix

### 6.1 RF Scatter Board Schematics & Bill of Materials

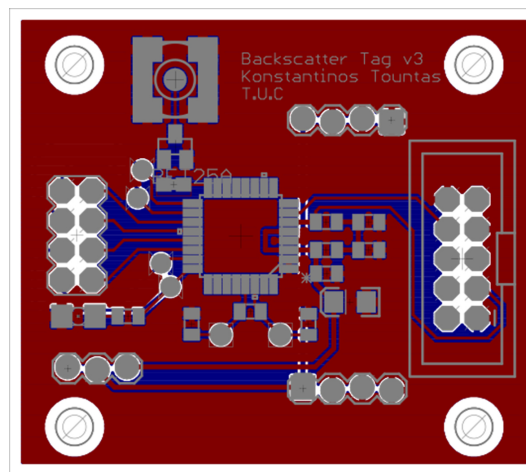
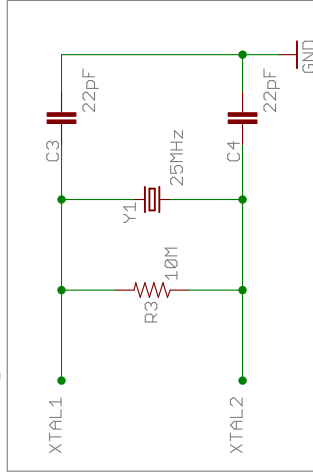
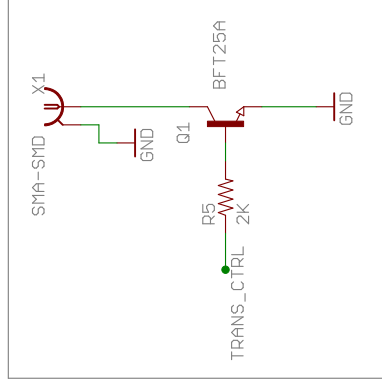
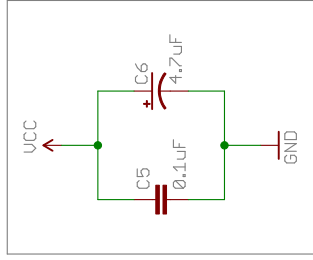


Figure 6.1: Scatter board layout.

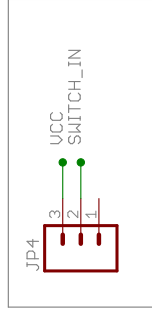
# Crystal Circuit



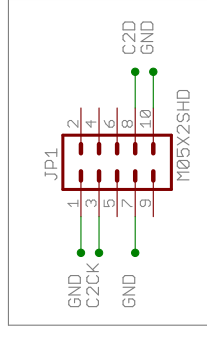
# Filter Circuit



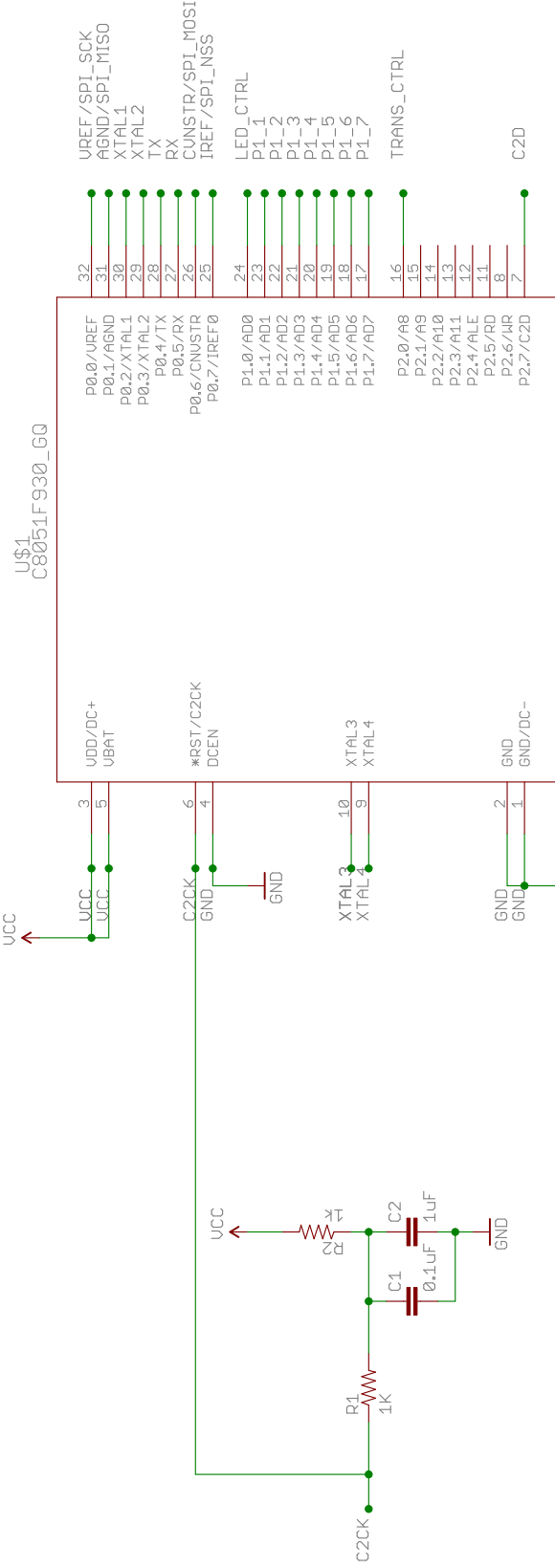
# RF Front End



# Switch



# Debug Adapter

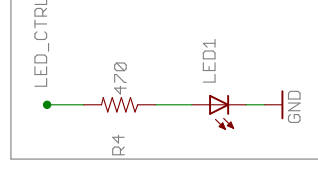
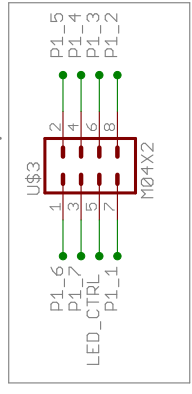


# MCU



# Power Board Input

# IO Adapter



# LED Circuit

Sheet1

## Scatter Tag V1

Quantity	Schematic	Man. Number	Description	Packaging	Value
2	C3, C4	C0805C220F5GACTU	CAP CER 22PF 50V 1% NP0 0805	0805	22 pF
1	C2	C0805C105K8RACTU	CAP CER 1UF 10V 10% X7R 0805	0805	1 uF
2	C1, C5	C0805C104K3RACTU	CAP CER 0.1UF 25V 10% X7R 0805	0805	0.1 uF
1	C6	T491A475K016AT	CAP TANT 4.7UF 16V 10% 1206	1206	4.7 uF
1	R3	CRCW080510M0DHEAP	RES SMD 10M OHM 0.5% 1/8W 0805	0805	10 Mohm
2	R1, R2	ERA-6AEB102V	RES SMD 1K OHM 0.1% 1/8W 0805	0805	1 Kohm
1	R4	ERA-6AEB471V	RES SMD 470 OHM 0.1% 1/8W 0805	0805	470 Ohm
1	R5	ERA-6AEB202V	RES SMD 2K OHM 0.1% 1/8W 0805	0603	2 Kohm
1	Y1	9B-25.000MAAI-B	Crystal 25.0000MHz 30ppm 16pF	Through Hole	-
1	Q1	BFT25A,215	TRANS NPN 5V 5GHZ SOT-23	SOT 23	-
1	X1	142-0711-201	CONN SMA JACK STR 50 OHM SMD	SMA-SMD	-
1	LED1	SML-LX1206GW-TR	LED 565NM GREEN DIFF 1206 SMD	1206	-
1	U1	C8051F930-G-GQ	IC MCU 8BIT 64KB FLASH 32LQFP	32-LQFN	-
1	JP4	EG1218	SWITCH SLIDE SPDT 30V.2A PC MNT	Through Hole	-

## 6.2 Power Board Schematics & Bill of Materials

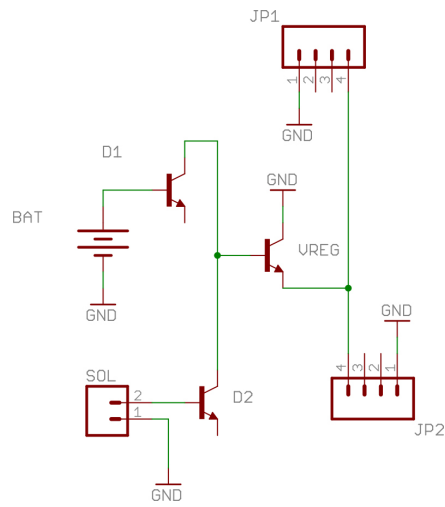


Figure 6.2: Power board schematic.

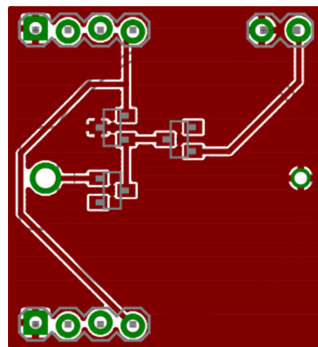


Figure 6.3: Power board layout.

# Power Board V1.0

Quantity	Schematic ID	Man. Number	Description	Packaging	Value
2	JP1, JP2	960114-6202-AR	Connector Receptacle 14 Position 0.100" Gold	Through Hole	-
1	VREG	REF3318A IDBZT	IC VREF SERIES 1.8V SOT23-3	SOT-23	-
2	D1, D2	BAT54-7-F	Diode Schottky 30V 200mA	SOT-23	-
1	BAT	BS-7	HOLDER COINCELL L 2032 RETAINER CLIP	DOM 20MM	-
1	SOL	961114-6404-AR	CONN HEADER VERT SGL 14POS GOLD	Through Hole	-

## 6.3 Sensor Board Schematics & Bill of Materials

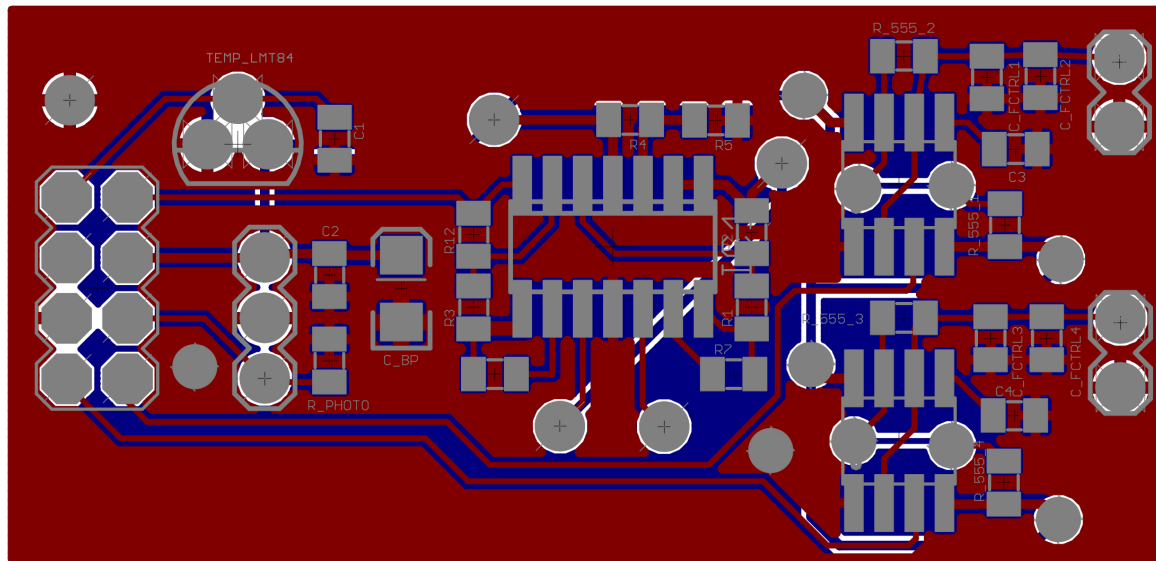
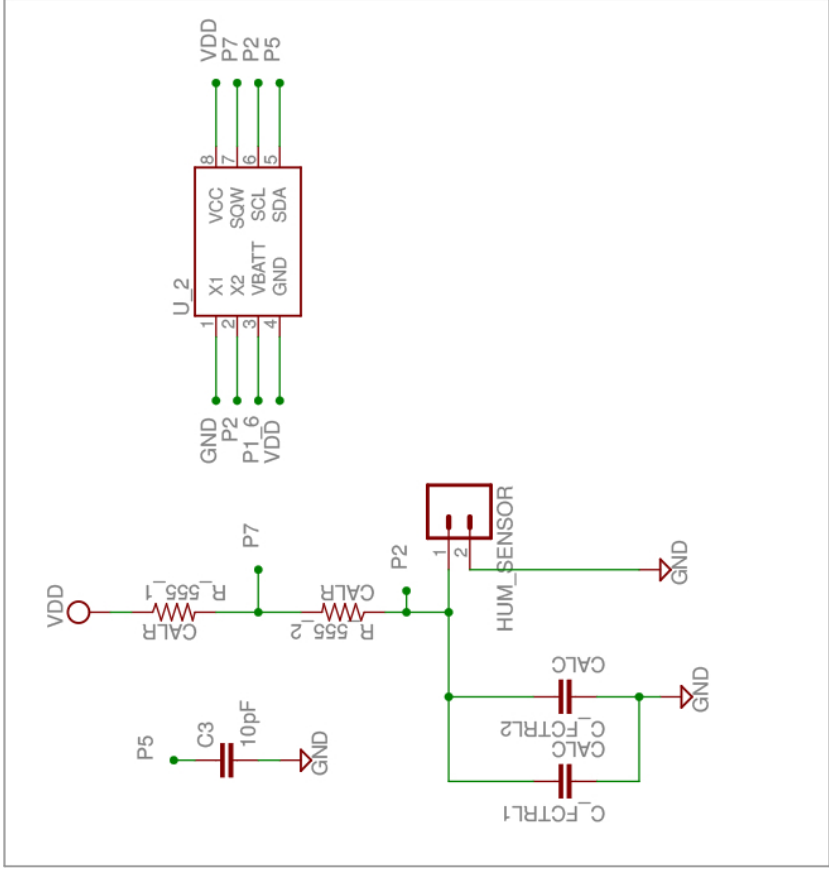
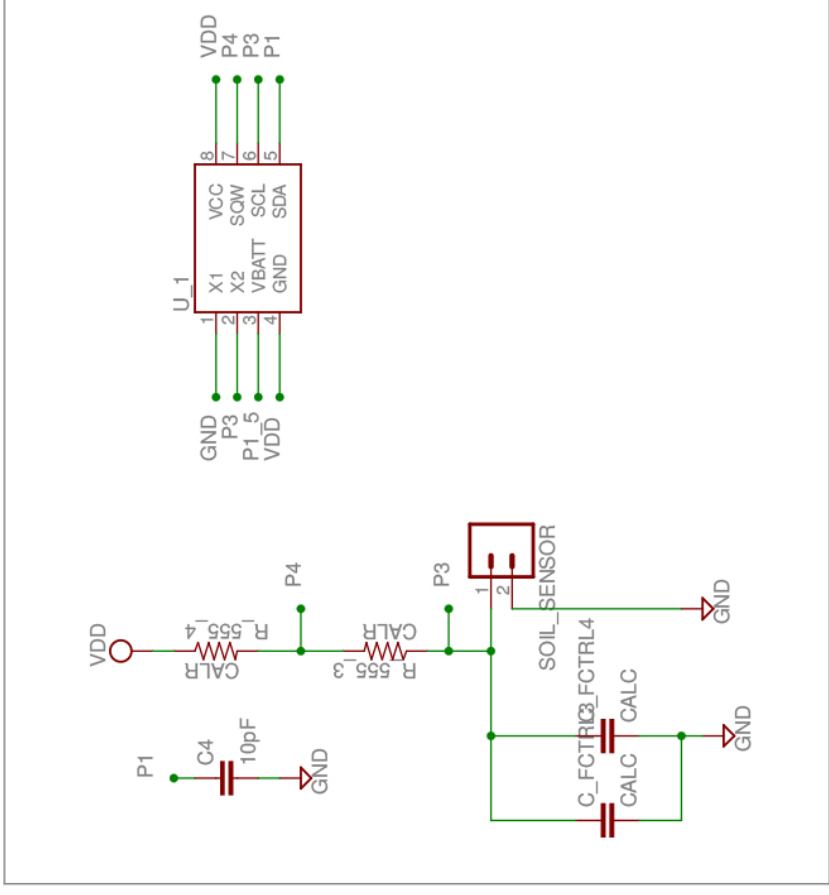


Figure 6.4: Sensor board layout.

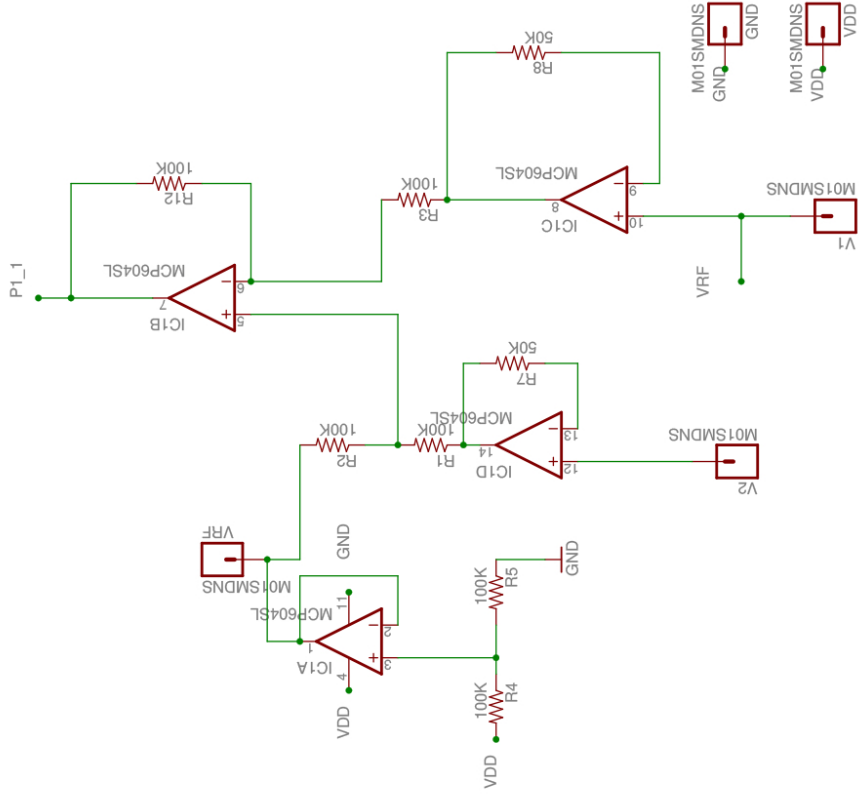


Humidity 555 Timer Circuit

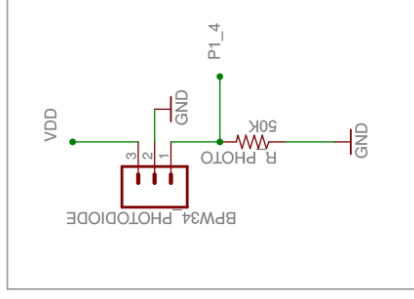


Humidity 555 Timer Circuit

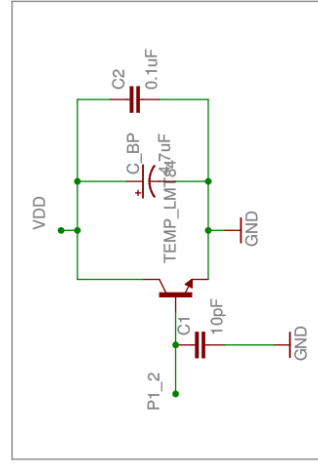
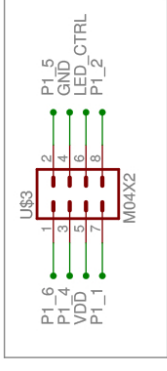
# Plant ECG Circuit



# Photodiode Circuit



# Tag Connector Circuit



# Temperature Sensor Circuit



# Bibliography

- [1] G. Vannucci, A. Bletsas, and D. Leigh, “A software-defined radio system for backscatter sensor networks,” *IEEE Trans. Wireless Commun.*, vol. 7, no. 6, pp. 2170–2179, Jun. 2008.
- [2] H. Stockman, “Communication by means of reflected power,” *Proc. IRE*, pp. 1196–1204, 1948.
- [3] K. Finkenzeller, *RFID Handbook: Fundamentals and Applications in Contactless Smart Cards and Identification*, 2nd ed. New York, NY: John Wiley and Sons, 2003.
- [4] J. Paradiso, L. Pardue, K. Hsiao, and A. Benbasat, “Electromagnetic tagging for electronic music interfaces,” in *Journal of New Music Research*, vol. 32, Dec. 2003, pp. 395–409.
- [5] J. Paradiso, K. Hsiao, and A. Benbasat, “Tangible music interfaces using passive magnetic tags,” in *ACM Conf. Human Factors in Computing Systems: Special Workshop on New Interfaces for Musical Expression*, Chicago, IL, 2001.
- [6] *EPC Radio-Frequency Identity Protocols, Class-1 Generation-2 UHF RFID Protocol for Communications at 860 MHz-960 MHz*. EPC Global, 2008, version 1.2.0.
- [7] A. P. Sample, D. J. Yeager, and J. R. Smith, “Design of a passively-powered, programmable sensing platform for UHF RFID systems,” in *Proc. IEEE Int. Conf. on RFID*, Grapevine, TX, Mar. 2007.
- [8] C. M. Kruesi, R. Vyas, and M. Tetzteris, “Design and development of a novel 3D cubic antenna for wireless sensor networks (WSN) and RFID applications,” *IEEE Trans. Antennas Propagat.*, vol. 57, no. 10, pp. 3293 – 3299, Oct. 2009.
- [9] V. Lakafosis, A. Rida, Y. Li, S. Nikolaou, and M. M. Tenteris, “Progress towards the first wireless sensor networks consisting of inkjet-printed, paper-based RFID-enabled sensor tags,” *Proc. IEEE*, vol. 98, pp. 1601–1609, Sep. 2010.
- [10] J. Kimionis, A. Bletsas, and J. N. Sahalos, “Increased range bistatic scatter radio,” *IEEE Trans. Commun.*, vol. 62, no. 3, pp. 1091–1104, Mar. 2014.

- 
- [11] E. Kampionakis, J. Kimionis, K. Tountas, C. Konstantopoulos, E. Koutroulis, and A. Bletsas, "Wireless environmental sensor networking with analog scatter radio & timer principles," *IEEE Sensors J.*, vol. 14, no. 10, pp. 3365–3376, Oct. 2014.
- [12] J. Griffin and G. Durgin, "Complete link budgets for backscatter-radio and RFID systems," *IEEE Antennas Propagat. Mag.*, vol. 51, no. 2, pp. 11–25, Apr. 2009.
- [13] N. Fasarakis-Hilliard, P. N. Alevizos, and A. Bletsas, "Coherent detection and channel coding for bistatic scatter radio sensor networking," *IEEE Trans. Commun.*, vol. 63, pp. 1798–1810, May 2015.
- [14] P. N. Alevizos, N. Fasarakis-Hilliard, K. Tountas, N. Agadakos, N. Kargas, and A. Bletsas, "Channel coding for increased range bistatic backscatter radio: Experimental results," in *Proc. IEEE RFID Techn. and Applications (RFID-TA)*, Tampere, Finland, Sep. 2014, pp. 38–43.
- [15] P. N. Alevizos and A. Bletsas, "Noncoherent composite hypothesis testing receivers for extended range bistatic scatter radio WSNs," in *Proc. IEEE Int. Conf. on Commun. (ICC)*, London, U.K., Jun. 2015.
- [16] A. Sample, J. Braun, A. Parks, and J. Smith, "Photovoltaic enhanced UHF RFID tag antennas for dual purpose energy harvesting," in *Proc. IEEE Int. Conf. on RFID*, Orlando, FL, Apr. 2011, pp. 146–153.
- [17] S. N. Daskalakis, S. D. Assimonis, E. Kampionakis, and A. Bletsas, "Soil moisture scatter radio networking with low power," *IEEE Trans. Microwave Theory Tech.*, vol. 64, no. 7, pp. 2338–2346, Jul. 2016.
- [18] D. Donno, F. Ricciato, L. Catarinucci, and L. Tarricone, "Challenge: towards distributed rfid sensing with software-defined radio," in *Proc. ACM Int. Conf. on Mobile Computing and Networking (Mobicom)*, New York, NY, 2010, pp. 97–104.
- [19] J. Griffin and G. D. Durgin, "Link envelope correlation in the backscatter channel," *IEEE Commun. Lett.*, vol. 11, no. 9, pp. 735–737, Sep. 2007.
- [20] A. Bletsas, A. G. Dimitriou, and J. N. Sahalos, "Improving backscatter radio tag efficiency," *IEEE Trans. Microwave Theory Tech.*, vol. 58, no. 6, pp. 1502–1509, Jun. 2010.
- [21] L. Zheng and D. N. C. Tse, "Diversity and multiplexing: A fundamental tradeoff in multiple antenna channels," *IEEE Trans. Inform. Theory*, vol. 49, no. 5, pp. 1073–1096, May 2003.

- 
- [22] D. Tse and P. Viswanath, *Fundamentals of Wireless Communication*. New York, NY: Cambridge University Press, 2005.
- [23] F. W. J. Olver, D. W. Lozier, R. F. Boisvert, and C. W. Clark, *NIST handbook of mathematical functions*. New York, NY: Cambridge Univ. Press, 2010.
- [24] I. S. Gradshteyv and I. M. Ryzhik, *Table of Integrals, Series, and Products*, 7th ed. Elsevier/Academic Press, Amsterdam, 2007.
- [25] A. Pappoulis and S. U. Pillai, *Probability, Random Variables and Stochastic Processes*, 4th ed. New York, NY: McGraw-Hill, 2002.
- [26] B. C. Levy, *Principles of Signal Detection and Parameter Estimation*. New York: Springer, 2008.